Buckling Testing and Analysis of Honeycomb Sandwich Panel Arc Segments of a Full-Scale Fairing Barrel

Part 1: 8-Ply In-Autoclave Facesheets

David E. Myers and Evan J. Pineda
Glenn Research Center, Cleveland, Ohio

Bart F. Zalewski
ZIN Technologies, Middleburg Heights, Ohio

Daniel N. Kosareo
Vantage Partners, LLC, Brook Park, Ohio

Sotiris Kellas
Langley Research Center, Hampton, Virginia

NASA STI Program . . . in Profile

Since its founding, NASA has been dedicated to the advancement of aeronautics and space science. The NASA Scientific and Technical Information (STI) program plays a key part in helping NASA maintain this important role.

The NASA STI Program operates under the auspices of the Agency Chief Information Officer. It collects, organizes, provides for archiving, and disseminates NASA's STI. The NASA STI program provides access to the NASA Aeronautics and Space Database and its public interface, the NASA Technical Reports Server, thus providing one of the largest collections of aeronautical and space science STI in the world. Results are published in both non-NASA channels and by NASA in the NASA STI Report Series, which includes the following report types:

- TECHNICAL PUBLICATION. Reports of completed research or a major significant phase of research that present the results of NASA programs and include extensive data or theoretical analysis. Includes compilations of significant scientific and technical data and information deemed to be of continuing reference value. NASA counterpart of peer-reviewed formal professional papers but has less stringent limitations on manuscript length and extent of graphic presentations.

- TECHNICAL MEMORANDUM. Scientific and technical findings that are preliminary or of specialized interest, e.g., quick release reports, working papers, and bibliographies that contain minimal annotation. Does not contain extensive analysis.

- CONTRACTOR REPORT. Scientific and technical findings by NASA-sponsored contractors and grantees.

- CONFERENCE PUBLICATION. Collected papers from scientific and technical conferences, symposia, seminars, or other meetings sponsored or cosponsored by NASA.

- SPECIAL PUBLICATION. Scientific, technical, or historical information from NASA programs, projects, and missions, often concerned with subjects having substantial public interest.

- TECHNICAL TRANSLATION. English-language translations of foreign scientific and technical material pertinent to NASA's mission.

Specialized services also include creating custom thesauri, building customized databases, organizing and publishing research results.

For more information about the NASA STI program, see the following:

- Access the NASA STI program home page at *http://www.sti.nasa.gov*

- E-mail your question to *help@sti.nasa.gov*

- Fax your question to the NASA STI Information Desk at 443–757–5803

- Phone the NASA STI Information Desk at 443–757–5802

- Write to:
  STI Information Desk
  NASA Center for AeroSpace Information
  7115 Standard Drive
  Hanover, MD 21076–1320
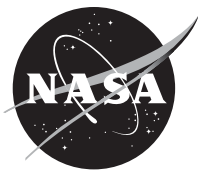
Buckling Testing and Analysis of Honeycomb Sandwich Panel Arc Segments of a Full-Scale Fairing Barrel

Part 1: 8-Ply In-Autoclave Facesheets

David E. Myers and Evan J. Pineda
Glenn Research Center, Cleveland, Ohio

Bart F. Zalewski
ZIN Technologies, Middleburg Heights, Ohio

Daniel N. Kosareo
Vantage Partners, LLC, Brook Park, Ohio

Sotiris Kellas
Langley Research Center, Hampton, Virginia

National Aeronautics and
Space Administration

Glenn Research Center
Cleveland, Ohio 44135

April 2013

Level of Review: This material has been technically reviewed by technical management.

Buckling Testing and Analysis of Honeycomb Sandwich Panel Arc Segments of a Full-Scale Fairing Barrel
Part 1: 8-Ply In-Autoclave Facesheets

David E. Myers and Evan J. Pineda
National Aeronautics and Space Administration
Glenn Research Center
Cleveland, Ohio 44135

Bart F. Zalewski
ZIN Technologies
Middleburg Heights, Ohio 44130

Daniel N. Kosareo
Vantage Partners, LLC
Brook Park, Ohio 44142

Sotiris Kellas
National Aeronautics and Space Administration
Langley Research Center
Hampton, Virginia 23681

Abstract

Four honeycomb sandwich panels, representing 1/16th arc segments of a 10-m diameter barrel section of the heavy lift launch vehicle, were manufactured under the NASA Composites for Exploration program and the NASA Space Launch Systems program. Two configurations were chosen for the panels: 6-ply facesheets with 1.125 in. honeycomb core and 8-ply facesheets with 1.000 in. honeycomb core. Additionally, two separate carbon fiber/epoxy material systems were chosen for the facesheets: in-autoclave IM7/977-3 and out-of-autoclave T40-800b/5320-1. Smaller 3.00- by 5.00-ft panels were cut from the 1/16th barrel sections. These panels were tested under compressive loading at the NASA Langley Research Center. Furthermore, linear eigenvalue and geometrically nonlinear finite element analysis was performed to predict the compressive response of the 3.00- by 5.00-ft panels. This manuscript summarizes the experimental and analytical modeling efforts pertaining to the panel composed of 8-ply, IM7/977-3 facesheets (referred to Panel A). To improve the robustness of the geometrically nonlinear finite element model, measured surface imperfections were included in the geometry of the model. Both the linear and nonlinear models yield good qualitative and quantitative predictions. Additionally, it was predicted correctly that the panel would fail in buckling prior to failing in strength. Furthermore, several imperfection studies were performed to investigate the influence of geometric imperfections, fiber misalignments, and three-dimensional (3–D) effects on the compressive response of the panel.

1.0   Introduction

Two manufacturing demonstration honeycomb sandwich panels (1/16th arc segments of 10.0 m diameter cylinder) were fabricated under the NASA Composites for Exploration (CoEx) program and two under the NASA Space Launch Systems (SLS) program. All four panels were manufactured by Hitco Carbon Composites. Two distinct configurations were chosen for the panels. The first configuration, fabricated under the CoEx program, was composed of 8-ply facesheets with a [45°/90°/–45°/0°]$_s$ lay-up and 1.000 in. aluminum (Al) honeycomb core. The second configuration, fabricated under the SLS

program, consisted of 6-ply facesheets with a [60°/-60°/0°]$_s$ stacking sequence and a 1.125 in. Al honeycomb core. In addition to the two configurations, two different carbon fiber/epoxy facesheet material systems were chosen for the panels: in-autoclave IM7/977-3 and out-of-autoclave (OOA) T40-800b/5320-1. It should also be noted that the honeycomb used in the 8-ply panels was machined to match the curvature of the panel while the honeycomb used in the 6-ply panels was flat. Additionally, in each panel, an adhesive splice joint was used to join discontinuous sections of the honeycomb core.

Following nondestructive evaluation (NDE) inspection, one 3.00- by 5.00-ft long section was machined from each full manufacturing demonstration panel for edgewise compression buckling tests. Following removal of the 3.00- by 5.00-ft panels from the manufacturing demo and after delivery to NASA Langley Research Center (LaRC), the panels were re-inspected using infrared (IR) Thermography to ensure that no damage had occurred. In preparation for testing, the load introduction ends of the panels were potted in 1.000-in thick Al end plates. The purpose of the end plates was to stabilize the facesheets and prevent local crushing, thus generating a predictable and repeatable end condition. Preliminary finite element analysis (FEA) indicated that no additional reinforcement was needed at the load introduction ends of the panels. A summary of the four 3.00- by 5.00-ft panels that were tested is given in Table I.

TABLE I.—DETAILS OF FOUR 5.00-ft TALL BY 3.00-ft WIDE PANELS CUT FROM 1/16th ARC SEGMENTS OF 10.0 m BARREL SECTION THAT WERE LOADED UNTIL BUCKLING

3- by 5-ft panel I.D.	1/16th arc segment panel I.D.	Facesheet material	Facesheet lay-up	Core thickness, in.
Panel A	[a]8000-CMDP	IM7/977-3 (IA)	[45°/90°/–45°/0°]$_s$	1.000 (curved)
Panel B-1	[b]MTP-6003	IM7/977-3 (IA)	[60°/–60°/0°]$_s$	1.125 (flat)
Panel B-2	MTP-6000	IM7/977-3 (IA)	[60°/–60°/0°]$_s$	1.125 (flat)
Panel C	8010-CMDP	T40-800b/5320-1 (OOA)	[45°/90°/–45°/0°]$_s$	1.000 (curved)
Panel D	MTP-6010	T40-800b/5320-1 (OOA)	[60°/–60°/0°]$_s$	1.125 (flat)

[a]Composite Manufacturing Demonstration Panel (CMDP)
[b]Manufacturing Test Panel (MTP)

The current document provides details specifically pertaining to Panel A, which consisted of 8-ply facesheets composed of in-autoclave IM7/977-3 and a 1.000 in. honeycomb core. Similar, separate documents have been prepared for Panels B, C, and D. The remaining subsections of Section 1.0 summarize the experimental and modeling objectives pertaining to all four panels. Section 2.0 provides details on Panel A. Section 3.0 describes several approaches that were used to predict the buckling load of Panel A. The experimental and numerical results are presented in Section 4.0. Finally, additional sensitivity studies are presented in Section 5.0.

1.1   Test Objectives

The primary objective of the test is to measure the maximum compressive load carrying capability (buckling load) of each 3.00-ft wide by 5.00-ft long panel and to provide data for analysis correlation and validation. A secondary objective is to study the effect of manufacturing defects on the deformation and buckling load.

1.2   Test Success Criteria

The test will be considered successful if each of the following criteria are met:

1. All critical instrumentation is fully operational during the test
2. The loads are applied as described in this document
3. Maximum attained load and all associated data are recorded and saved in the desired format

1.3   Modeling Objectives

The primary modeling objective is to predict the buckling load and structural response of each 3.00-ft wide by 5.00-ft long panel as accurately as possible using standard, commercially available, analysis tools. A linear eigenvalue baseline, obtained from the finite element method (FEM), will be compared to the experiment. More sophisticated, progressive collapse analyses, incorporating nonlinear geometric effects and the measured geometric imperfections of the panel surfaces, will be executed in an attempt to improve the baseline numerical (FEM) prediction. Additionally, linear strength analyses will be performed to ensure that predicted buckling occurs before expected strength failure. Finally, parametric studies will be performed to determine the sensitivity of the buckling load of the panel to varying degrees of imperfections including as manufactured geometry, fiber angle misalignment, and loading eccentricity.

1.4   Modeling Success Criteria

The modeling will be considered successful if each of the following criteria are met:

1. The buckling load is predicted within 20 percent
2. The buckling mode/direction is predicted accurately
3. Local strain fields correlate well qualitatively with visual imaging data measured during the experiment

2.0   1/16th Panel Description

The 1/16th fabrication demo panel was constructed on a concave composite tool (5.00 m radius of curvature) using an automated tape laying process. The pre-impregnated (prepreg) tape was composed of unidirectional fibers and was 6 in. wide. The prepreg contained IM7 fibers and 977-3 epoxy. The stacking sequence of the facesheets was $[45°/90°/–45°/0°]_s$. The facesheets were bonded to the 1-in. thick Al core using FM 300 film adhesive, 0.08 lb/ft^2. The Al honeycomb core was curved, via machining, to match the radius of the tool. The facesheets and core adhesive were co-cured in a single autoclave cycle. The Al core was Alcore PAA-CORE 5052, 0.000700-in. thick with 0.1250-in. cell size, and a density of 3.1 pcf. An adhesive splice was needed to join discontinuous sections of the core because the 1/16th barrel section panel dimensions exceeded the size of the premanufactured core. A Hysol 9396.6 foaming adhesive was used to fill the gap between the two pieces of Al core. A photograph of the manufacturing demonstration 1/16th arc segment (of a 5.00-m outside radius cylinder) panel is shown in Figure 1.

2.1   Test Specimen Description

One 36.00-in. wide by 62.00-in. long test specimen was machined from the manufacturing demo panel following nondestructive examination. The end plates were 1.000-in. thick Al plates and had a slot in the shape of the specimens cross section machined in the center. The slot width and length were such that, when centered, the specimen had a clearance of 0.5000 in around the perimeter. After the specimen-end was centered in the slot and squared, it was potted with "UNISORB" V-100 epoxy grout. When both ends were potted and following cure, specimen ends were machined flat and parallel to within ±0.002500 in. A photograph of the test specimen with potted ends is shown in Figure 2. The potted dimensions of the 977-3 panel are shown in Figure 3. In addition to the overall dimensions, Figure 3 shows the relative position of the core splice with respect to the panel ends. For complete details on the CoEx experimental efforts, the reader is referred to Kellas, et al. (2012).

Once potted, strain gages were affixed to the inner diameter (I.D.) and outer diameter (O.D.) surfaces of the panel, as shown in Figure 4. The even numbered gages were located on the I.D. while the odd numbered gages were located on the O.D. These gages were monitored and the strains were recorded during loading of the panel. The panel was tested at LaRC in a servo-hydraulic test frame. The panel was

secured between two loading platens, with the bottom loading platen being fixed and the top platen allowed to move in the y-direction. The panel was loaded in compression until catastrophic failure occurred. Additional instrumentation included three direct-current displacement transducers (DCDTs) used to measure the global, axial deformation of the panel, and a load cell attached to the load platen to measure the applied load. Finally, the panels were painted using a speckle pattern for photogrammetric measurements. Visual image correlation (VIC) was employed to obtain full-field strain measurements during the test as well as high speed video.

Figure 1.—Photograph of cured 1/16th arc segment panel and the tool it was molded on.
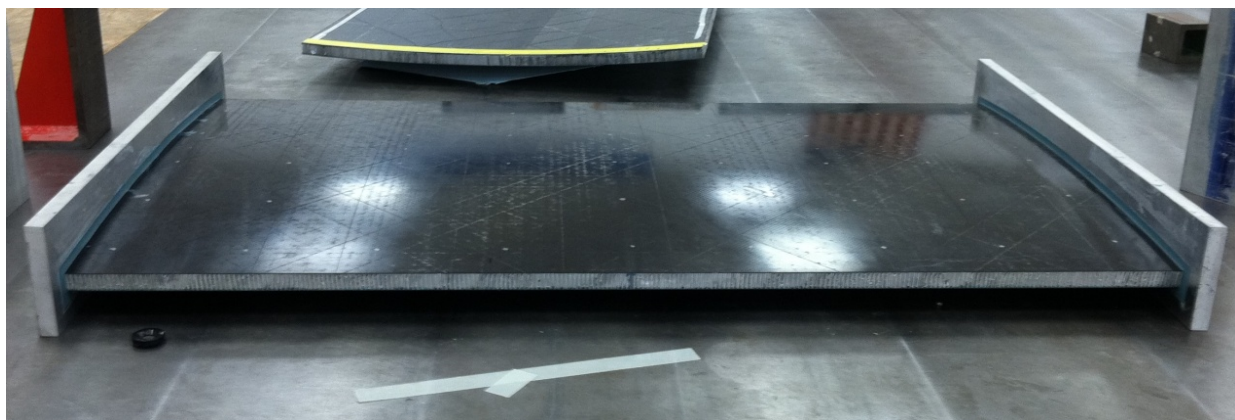
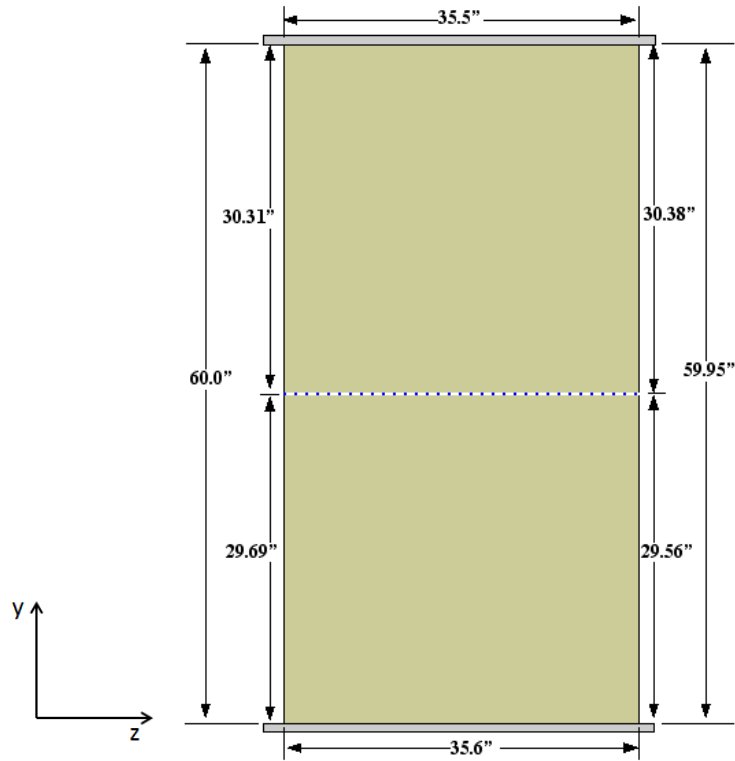Figure 2.—Photograph of the test panel with potted Al end plates.

Figure 3.—Potted specimen dimensions. Note that the outside surfaces of the Al end plates were machined flat and parallel. The position of the core splice is also shown relative to the inside surface of the Al end plates.
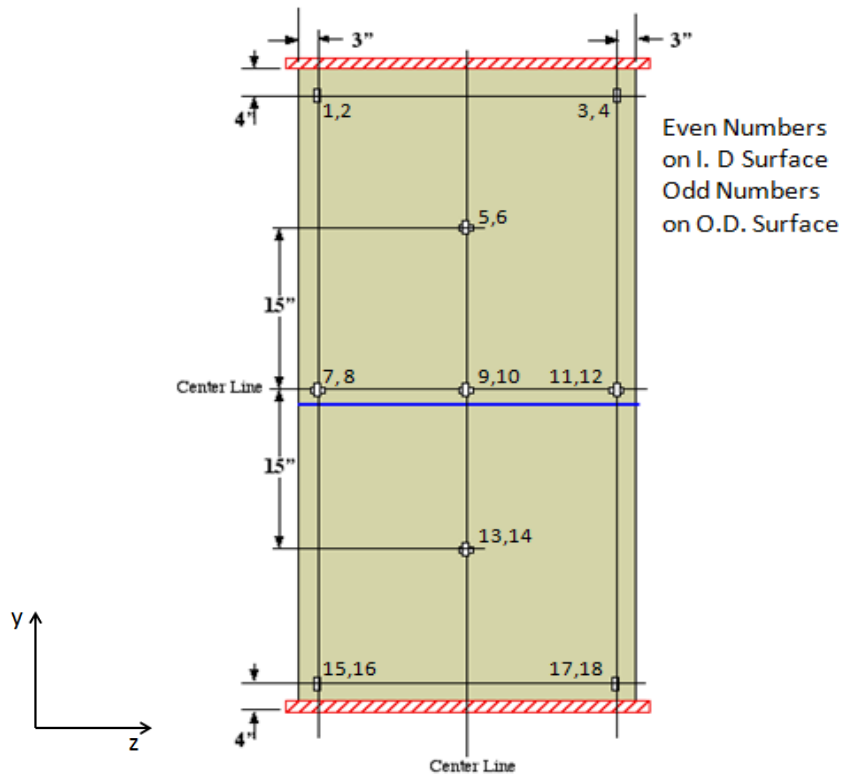

Even Numbers on I. D Surface Odd Numbers on O.D. Surface

Figure 4.—Panel geometry and strain gage location/nomenclature.

3.0   Finite Element Analysis Description

Pretest predictions of the buckling load for Panel A were determined using commercially available FEM software packages: MSC/NASTRAN, Abaqus, and ANSYS. Figure 5 shows the test panel geometry used in the FEM models. The panel was modeled as 60.00 in. tall (section between the Al end plates) and 35.50 in. along the arc (35.45 in. along the chord) using two-dimensional (2–D) layered shell elements. The 1.000 in. sections of the panel on the top and bottom that were supported in the potting material were not modeled. The element size was 1.000- by 0.9700-in., and the model was comprised of 2319 nodes and 2221 elements. All three displacements and all three rotations were fixed along the bottom edge of the panel. The same boundary condition was applied to the top edge, except a displacement was applied in the negative y-direction.

The stacking sequence of the facesheets was $[45°/90°/-45°/0°]_s$ with 0.0053 in. plies. The IM7/977-3 elastic properties and allowables (used in strength analysis) were obtained from the Orion materials database, and are not shown as they are ITAR restricted (Lockheed Martin, 2010). The Al honeycomb properties were obtained from the database included with the commercially available structural sizing software, HyperSizer, and are presented in Table II. The in-plane normal and shear stiffnesses were reduced from 75.0 ksi to 1.00×10^{-7} ksi since in-plane load carrying capability of the honeycomb is typically neglected in honeycomb sandwich panel analysis.
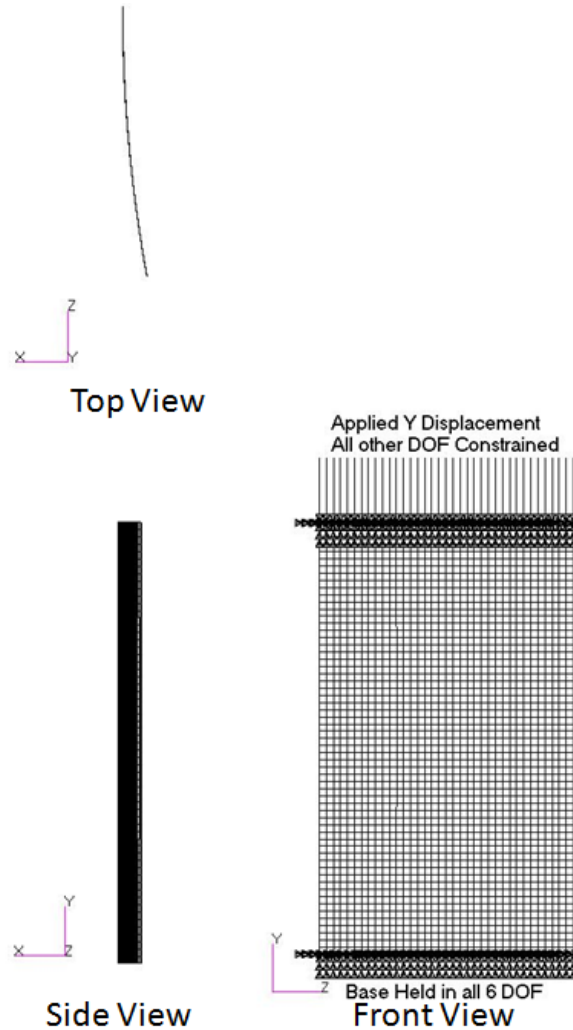

Figure 5.—Panel geometry with boundary conditions

TABLE II.—Al HONEYCOMB MATERIAL
PROPERTIES, 3.1 PCF, 1/8 in.-5052-0.0007

E_1, ksi	1.00×10^{-7}
E_2, ksi	1.00×10^{-7}
ν_{12}	0.333
G_{12}, ksi	1.00×10^{-7}
G_{1Z}, ksi	45.0
G_{2z}, ksi	22.0
ρ, pcf	3.10
F_{t1}, ksi	0.200
F_{c1}, ksi	0.200
F_{t2}, ksi	0.200
F_{c2}, ksi	0.200
F_{s12}, ksi	0.090

To arrive at a baseline buckling failure prediction, a linear eigenvalue buckling analysis (Sol 105) was performed in MSC/NASTRAN. This preliminary analysis was executed for two reasons. First, the analysis provides a reasonable estimate of what the nonlinear analysis should predict as the panel buckling load with an efficient, quick turnaround. Second, this is the typical method of calculating buckling loads for flight structures, and it is informative to compare the results to the experimental buckling load and the buckling loads obtained from higher-fidelity models.

In addition, to improve numerical predictions, it was also pertinent to predict which direction (towards the I.D. or O.D.) the panel would buckle as a DCDT was to be placed to measure the out-of plane displacement of the panel and severe displacement in the unexpected direction would damage the gage. The eigenvectors obtained from an eigenvalue analysis are in an arbitrary direction and do not indicate the direction the panel would buckle. Therefore, geometrically nonlinear static analyses were performed in MSC/NASTRAN (Sol 106), Abaqus, and ANSYS to arrive at a more accurate buckling load and determine the direction of buckling correctly.

Hause et al. (1998, 2000), Hilburger et al. (2001), Hilburger and Starnes, Jr. (2002), Lynch et al. (2004), Schultz and Nemeth (2010) have shown that FEM simulations of progressive collapse incorporating geometric nonlinearities are extremely sensitive to the geometric imperfections in the panel. Thus, it was desired to use some measure of the actual imperfections of the panel and include them in the model. Preliminary photogrammetry data of the panel showed that the bag side (I.D.) surface contained some initial imperfections that were biased towards the I.D. On the O.D., or the tool side, the surface imperfections were sinusoidal in nature. Herein, these surface imperfections are referred to as the bow shape of the panel. In the progressive collapse analyses, the bow data from the bag side of the panel was used to incorporate geometric imperfections into the model. Figure 6 shows the imperfection, or bow, data measured vertically from the top of the panel to the bottom of the panel at the horizontal center. The raw photogrammetry data was first rotated such that both the top and bottom had an out-of-plane bow displacement of 0.000 in. The data was then scaled (60.00-in./total height of photogrammetry data) so that it covered the full 60.00 in. of the panel. These two modifications resulted in the curve labeled "Photogrammetry – Mod" in Figure 6. The photogrammetry data was not used directly since there were local maxima that corresponded to the location of the strain gages that were already attached to the panel. These local maxima were ignored, and as shown on Figure 6, the curve labeled "NASTRAN Estimation" was used to approximate the bow shape in all models. The approximated bow geometry was then swept along an arc of radius 198.0 in. and 10.272°, providing a uniform tangential panel cross section. Realistically, the cross section of the panel varies in the circumferential direction, but it was assumed that the imperfect, but uniform, cross section used in the numerical model is sufficient to capture the primary effects of the geometric imperfections in the panel.
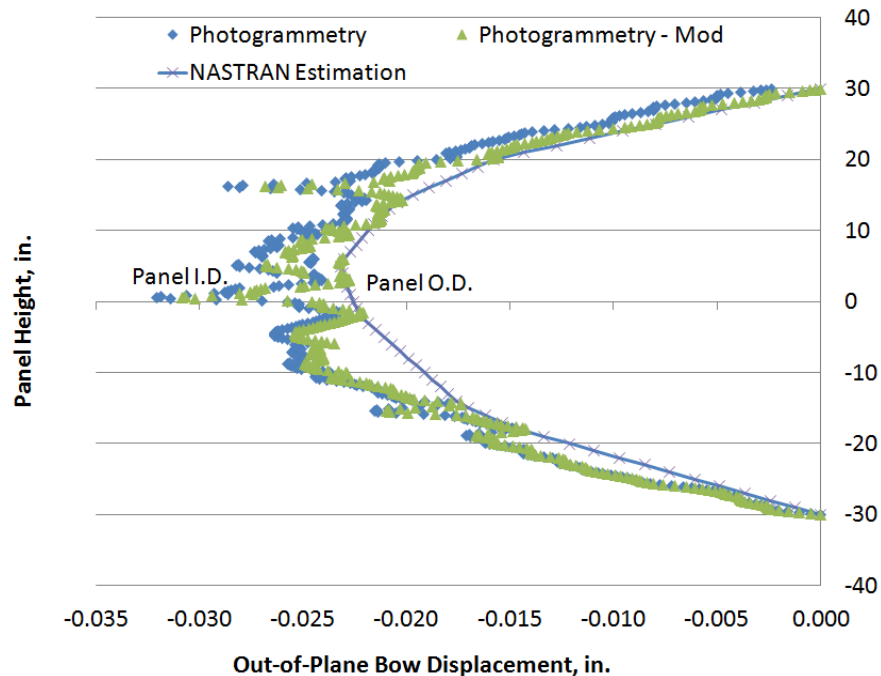
Figure 6.—Imperfection, or bow, data from the bag side (I.D.) of the panel. Data were taken vertically along the height of the panel, in the horizontal center of the panel.

Finally linear static solution in MSC/NASTRAN (Sol 101) was executed to determine the strength margins of safety at the time of onset of buckling. A similar analysis was performed in HyperSizer. These results were used to determine whether the failure of the panel was stiffness critical (buckling) or strength critical (local facesheet or core failure).

4.0   Test and Analysis Comparison

To determine the panel buckling load a method from Singer, et al. (1998), shown in Figure 7, was used. This method utilizes global load versus local strain gage data (axial strain) to mark the onset of buckling. In Figure 7, a vertical tangent line intersects the load-strain curve at a local strain where the local strain increment reverses which is designated the local buckling strain. The load corresponding to that local strain is designated the buckling load. It should be noted that the buckling strain, and hence buckling load, can only be determined at monitored locations and therefore can actually be lower than the lowest measured value. Thus, the postulated buckling load is somewhat subjective and based upon the location where the strains are being monitored for reversal. Test data for Gages 11 and 12 exhibited strain reversal at the lowest applied edge loads. This load, 72,100 lb, will be considered the buckling load, and the numerical buckling loads will be determined from the global load versus local strain plots obtained from points on the models corresponding to these gage locations.

4.1   Linear Buckling Analysis

A linear buckling analysis was performed using NASTRAN Sol 105. Figure 8 shows the eigenvector plot when –0.1980 in. was applied to the edge. The corresponding reaction load was 80,912 lb. Thus, the linear eigenvalue solution predicted a buckling load 12.2 percent higher than the test results. As mentioned before, the eigenvectors do not indicate the direction of buckling in a panel where there is a preferred direction, such as a curved panel.
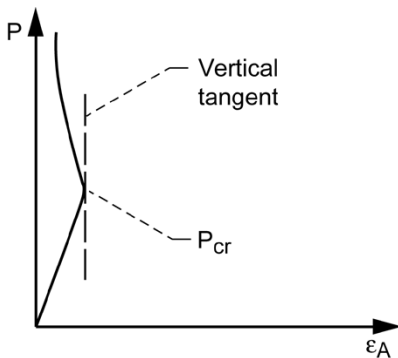
Figure 7.—Method for determining
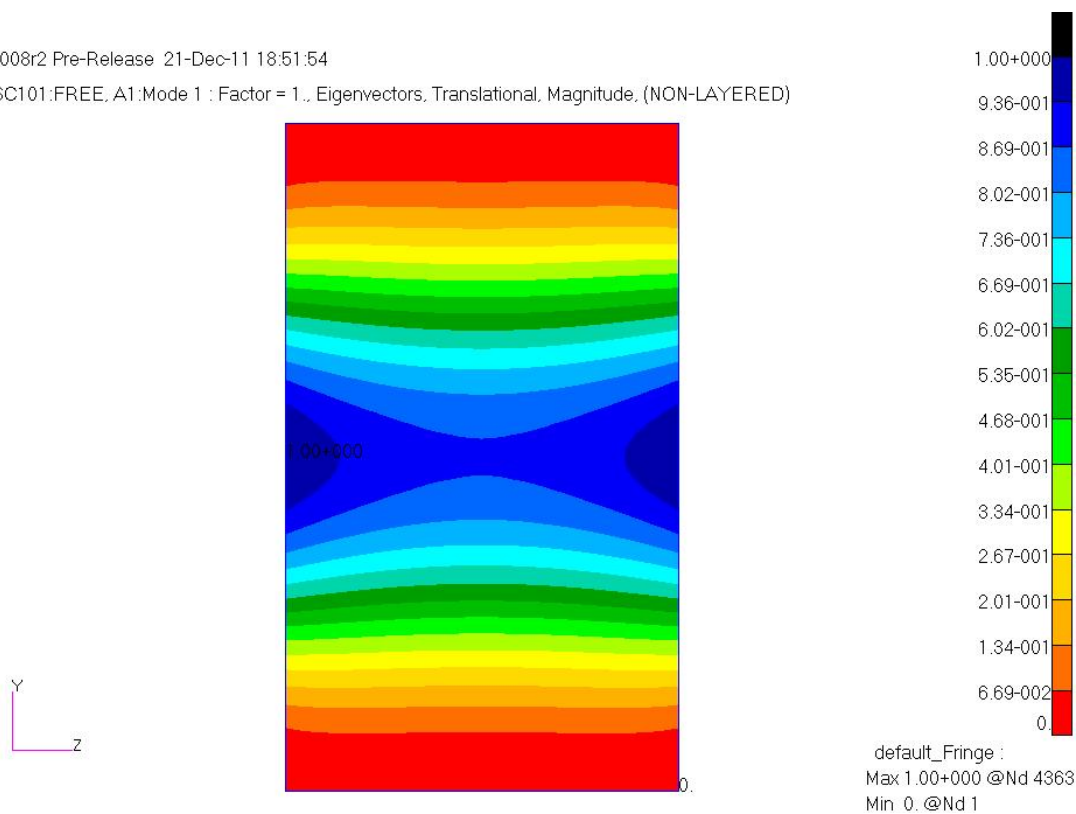buckling load, Singer, et al. (1998).

Figure 8.—Euler eigenvector buckling plot obtained from MSC/NASTRAN.

4.2   Nonlinear Buckling Analysis

To obtain a more accurate prediction of the buckling load, a pretest, geometrically nonlinear analysis was executed using MSC/NASTRAN Sol 106. For verification, several additional analyses, including implicit nonlinear static and dynamic MSC/NASTRAN (Sol 600), static nonlinear ANSYS, and static nonlinear Abaqus, were completed. Note that the ANSYS model included both the approximated imperfection geometry presented in Figure 6 and was seeded using the mode shapes from a preliminary, linear eigenvalue buckling analysis. For complete details on the ANSYS analysis, please refer to Section 5.3. Table III summarizes details of the various analysis tools that were used to predict the buckling load of the panel. Figure 9 shows the load-deflection curves for all analyses as well as the experiment, while Figure 10 and Figure 11 show the same data in a less cluttered format. The figures

show that Abaqus more closely match the test data while the other solutions are slightly less conservative, taking their load-deflection curves further above the test data.

TABLE III.—SUMMARY OF ANALYSIS TOOLS USED TO PREDICT BUCKLING RESPONSE OF SANDWICH PANEL

Software	Solution	Description	Imperfection Seeding
MSC/NASTRAN	105	Linear eigenvalue solution	Approximated bow
MSC/NASTRAN	106	Static solution with nonlinear geometry	Approximated bow
MSC/NASTRAN	600	Static and implicit dynamic solution with nonlinear geometry	Approximated bow
Abaqus	Static, NLGEOM	Static solution with nonlinear geometry	Approximated bow
ANSYS	Static, NLGEOM	Static solution with load increments and nonlinear geometry	Mode shapes and approximated bow
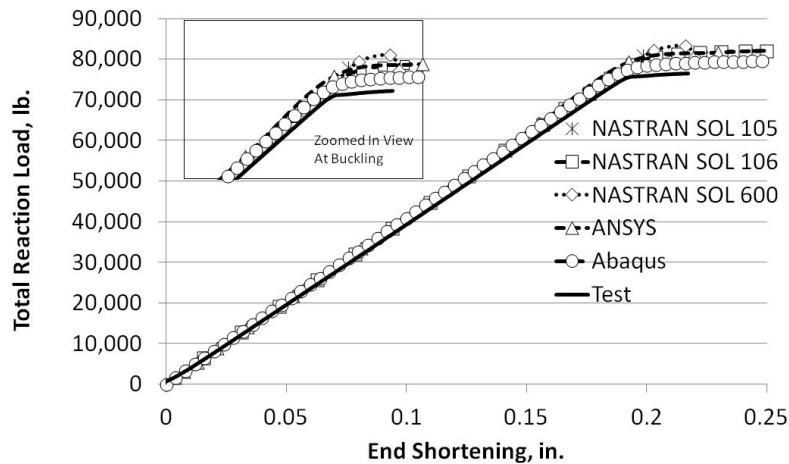
Figure 9.—Total reaction load versus end shortening for all analyses.
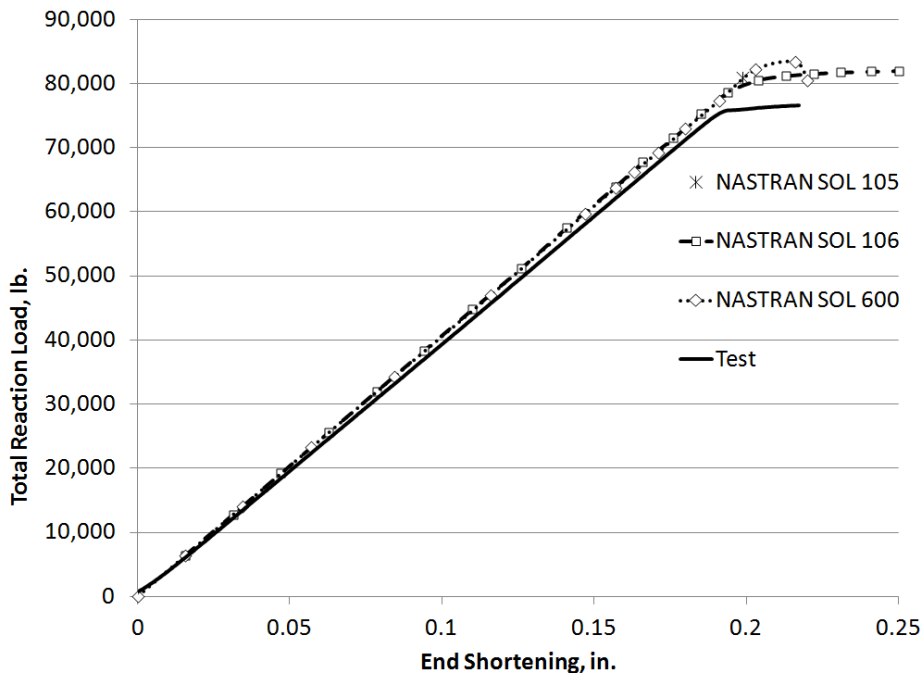
Figure 10.—Total reaction load versus end shortening for Sols 105, 106, and 600 and test.
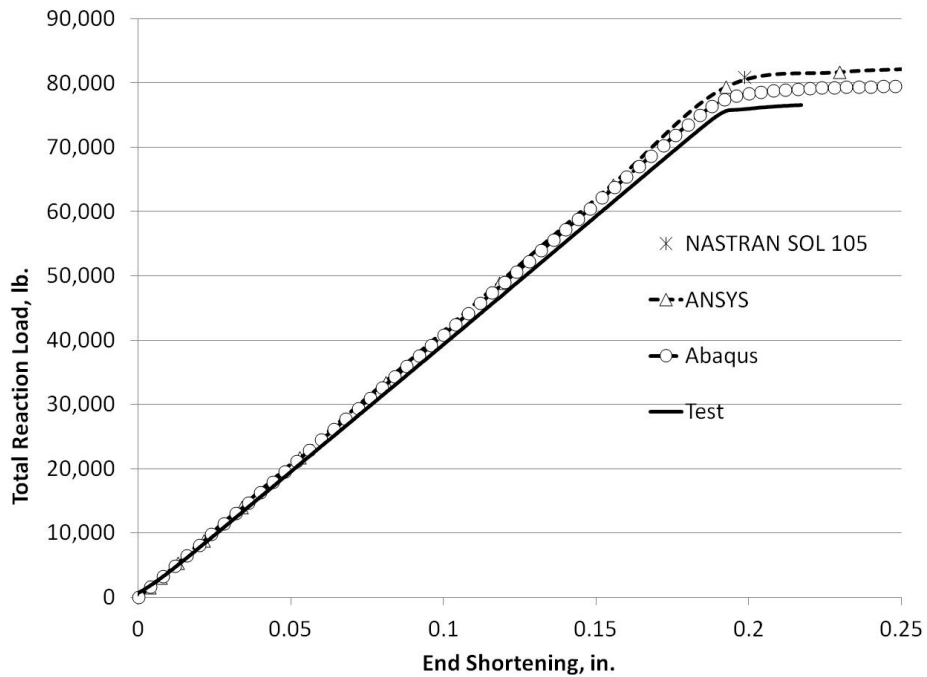
Figure 11.—Total reaction load versus end shortening for Sols 105, ANSYS, Abaqus, and test.
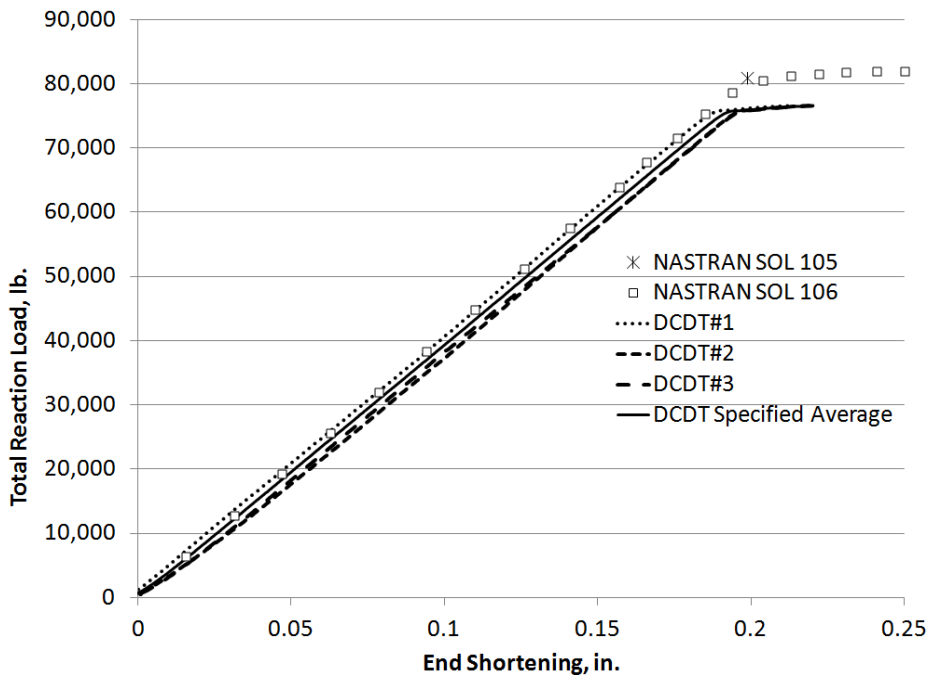
Figure 12.—DCDT end shortening versus total reaction load.

In all the analyses the linear prebuckling panel stiffness was nearly the same. However, the stiffness obtained from the analyses was slightly higher than the test stiffness. Figure 12 shows the measurements of all three DCDTs that were affixed to the panel during loading. DCDT#1 aligned almost perfectly with the NASTRAN Sol 106 results (the most over-predicted results) while DCDT#2 and #3 showed lower stiffnesses, yielding an average measurement that produces a lower stiffness than the analytical

predictions. Additionally, there is some initial nonlinearity in the DCDT results. This indicates that there is some settling due to contact as the panel is initially loaded. The slopes of the "NASTRAN SOL 106," DCDT#1," "DCDT#2," "DCDT#3," and "DCDT Specified Average" curves are presented in Table IV at an end shortening of 0.1 in. (to eliminate settling). The analytical predicted stiffness was slightly above all three independent DCDT readings. Thus, additional sources of discrepancy between the stiffness of the FEM model and the experiment may be due to machine compliance, slight misalignments of the fibers within the plies to the intended ply angle, or variation in the fiber volume fraction/actual thickness of the plies resulting from the curing process. Results from a sensitivity study on fiber misalignment are presented in Section 5.2. In addition, results from a sensitivity study on three dimensional effects using ANSYS are presented in Section 5.3.

For simplification, only analytical results obtained from MSC/NASTRAN will be presented in the remainder of this section (Section 4.2). Figure 13 shows the out-of-plane displacement contour plot and deformed shape obtained from analysis, at an applied edge displacement of –0.2500 in., well into the post-buckled regime. This plot displays that panel buckling was predicted towards the I.D, which is consistent with the buckling direction observed in the experiment.

TABLE IV.—TANGENT SLOPES OF CURVES IN
FIGURE 12 AT AN END SHORTENING OF 0.1 in.

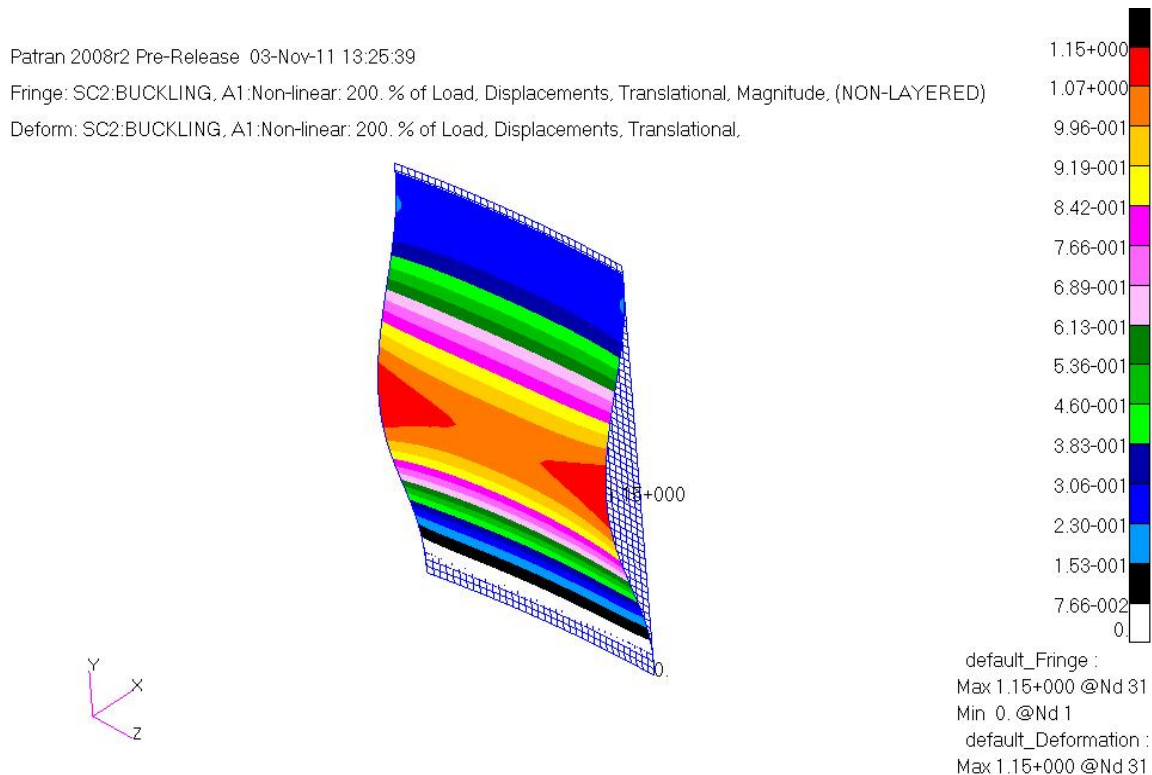| Curve	Slope, kips/in.
NASTRAN SOL 106	404.8
DCDT#1	402.2
DCDT#2	396.6
DCDT#3	395.7
DCDT Specified Average	398.2

Figure 13.—Panel displacement plot for –0.25 in. applied edge displacement.

The buckling load determined using the highest strain located at the vertical center of the panel near the edges was 75,235 lb. Loads corresponding to all strain gage locations are tabulated with the experimental values in Table V. Figure 14 and Figure 15 show that, in the corner, the axial O.D. panel strain goes into compression up to the onset buckling, after which the strain increment reverses and the axial strain is alleviated as the load increases during post-buckling. This local behavior (observed both experimentally and numerically) is consistent as the panel buckled towards the I.D. Note that, since the major curvature of the panel is biased towards the O.D., the analysis would predict buckling towards the O.D. if no geometric imperfections (bow) were introduced into the model. Figure 16 shows the strain gage measurements at a panel inflection point at the ¾ panel length location. Figure 17 to Figure 19 show that at the horizontal center of the panel, the I.D. panel strain goes into compression up to buckling and then reverses as the load increases during post-buckling. The results from Figure 20 the lower inflection or ¼ length location, match the results from Figure 16 while the results from Figure 21 and Figure 22 match the results from Figure 14 and Figure 15, respectively. The error in the nonlinear analysis ranges from 4.4 percent (Table V), which was a significant improvement over the linear analysis.

TABLE V.—APPROXIMATE TEST AND ANALYSIS PREDICTION BUCKLING LOADS
[See Figure 4 for gage locations on panel]

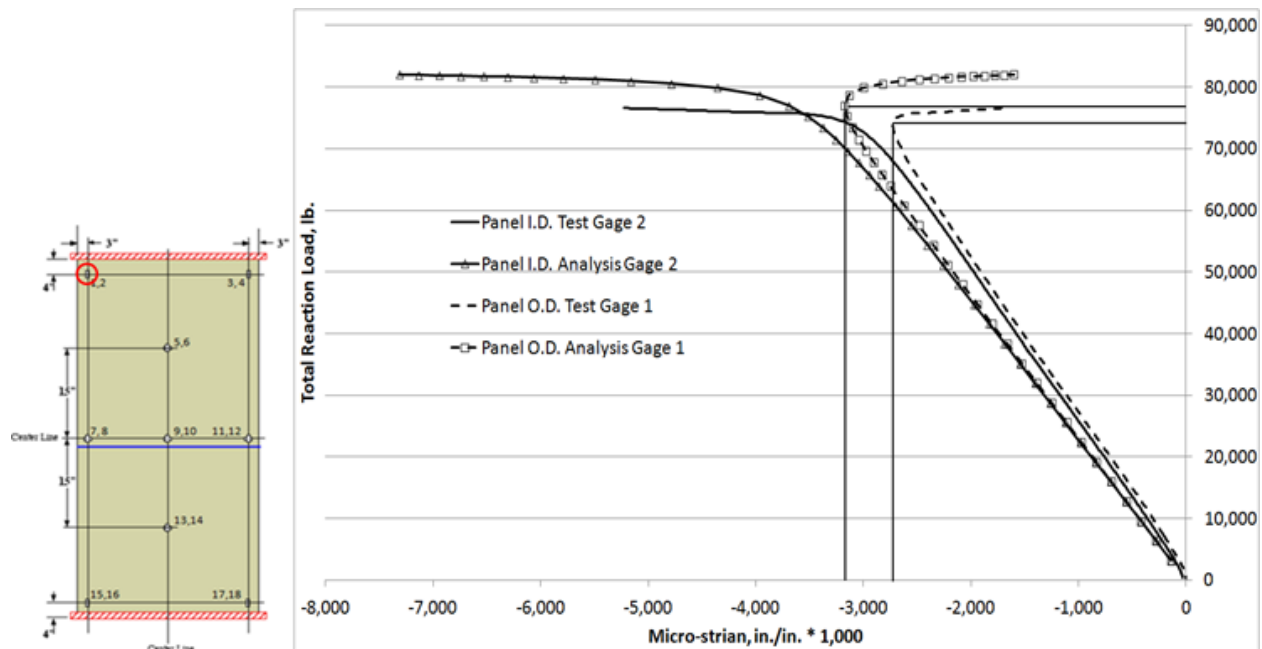| Gage	Test, lb	Analysis, lb	Error, %
1, 2	73,420	77,040	4.9
3, 4	73,870	77,040	4.3
7, 8	72,170	75,235	4.2
9, 10	73,560	77,040	4.5
11, 12	72,100	75,235	4.3
15, 16	73,630	77,040	4.6
17, 18	73,740	77,040	4.5

Figure 14.—Load/strain plot for gages 1 and 2, upper left corner of panel (see Figure 4). Analysis obtained from MSC/NASTRAN, Sol 106.
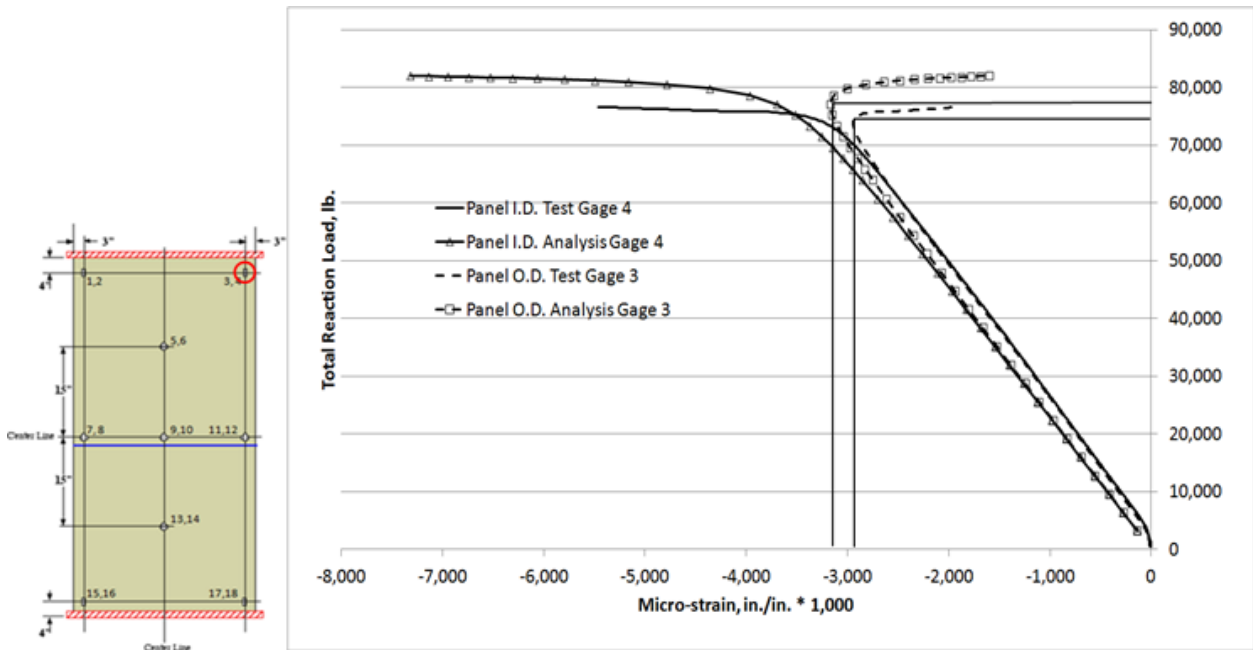
Figure 15.—Load/strain plot for gages 3 and 4, upper right corner of panel (see Figure 4). Analysis obtained from MSC/NASTRAN, Sol 106.
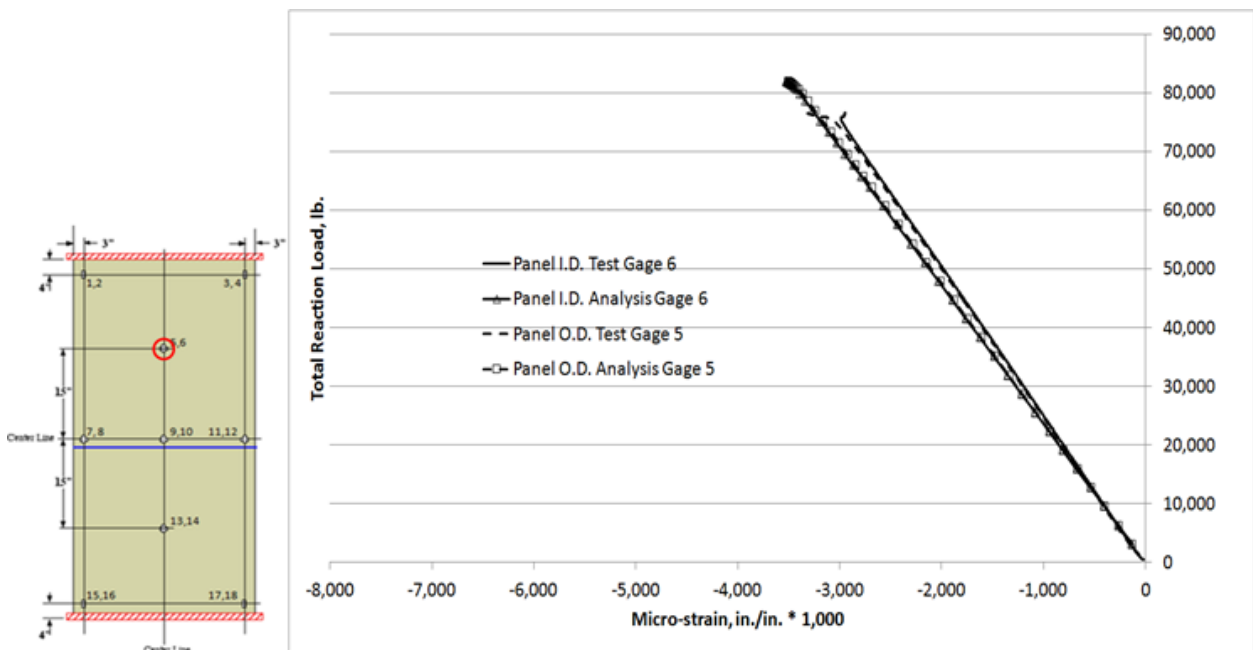

Figure 16.—Load/strain plot for gages 5 and 6, at panel inflection point, ¾ length (see Figure 4). Analysis obtained from MSC/NASTRAN, Sol 106.
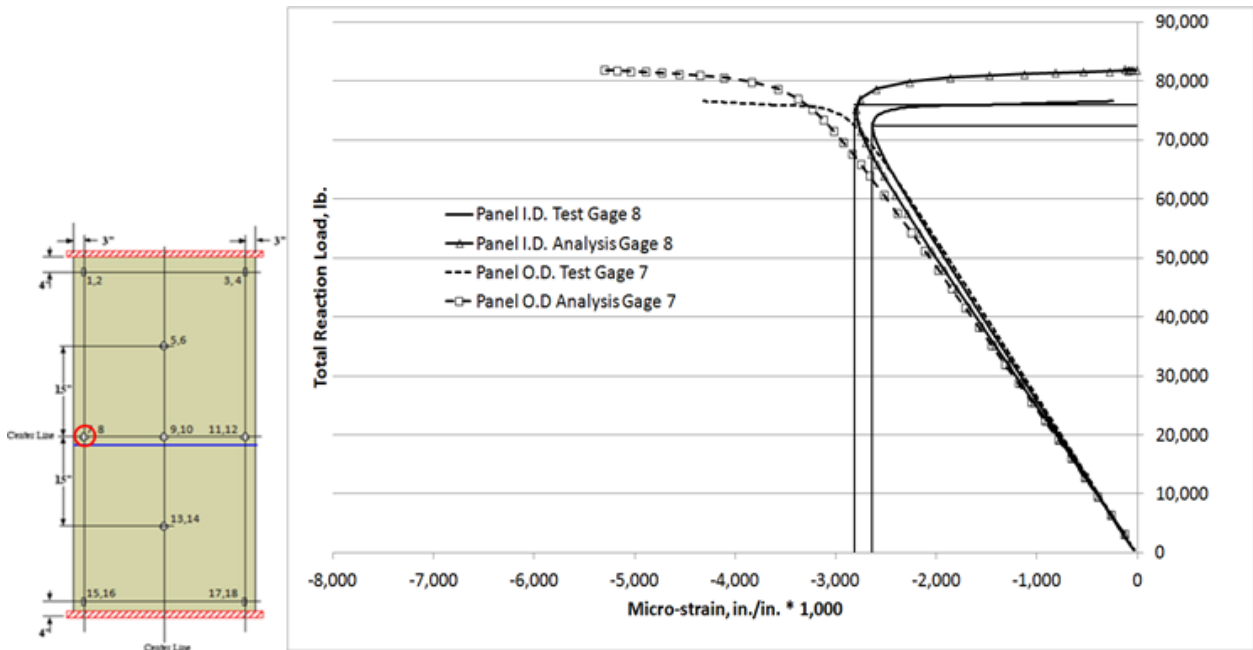
Figure 17.—Load/strain plot for gages 7 and 8, at horizontal left side (see Figure 4). Analysis obtained from MSC/NASTRAN, Sol 106.
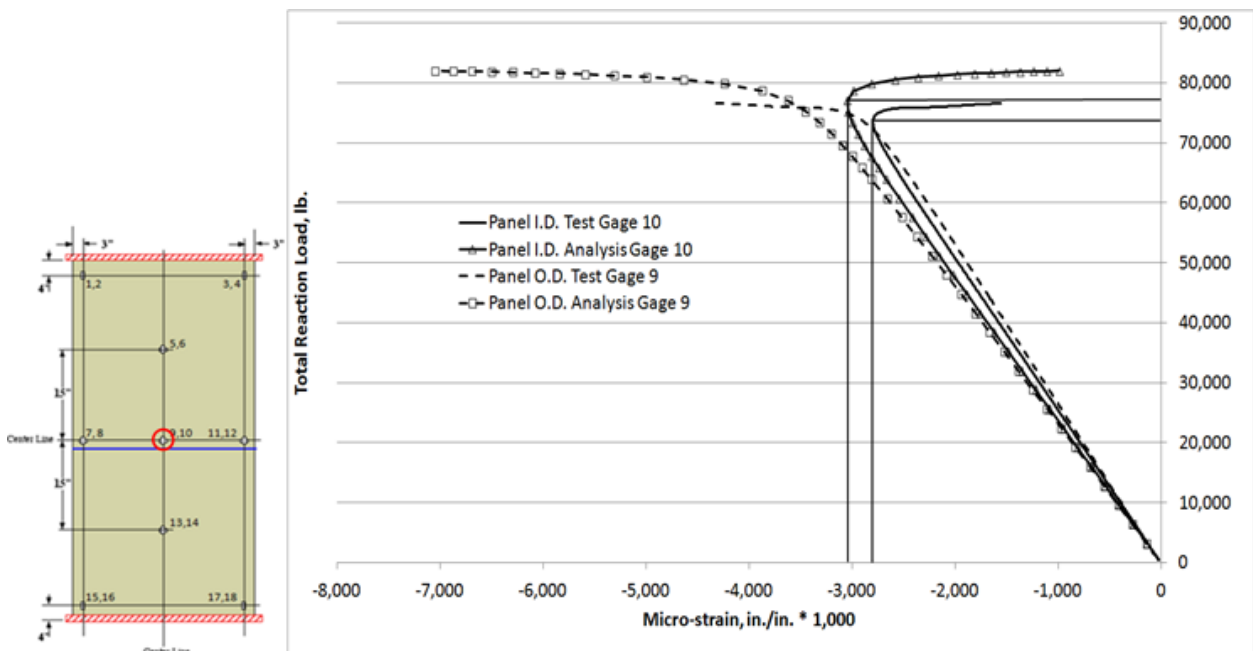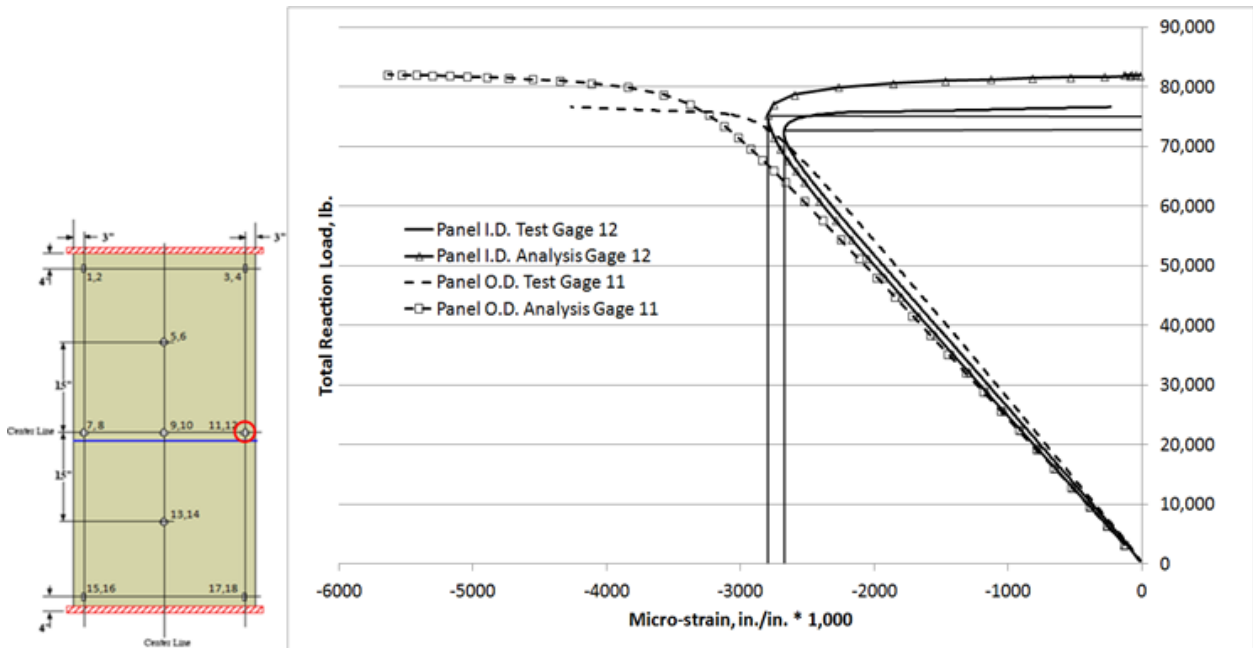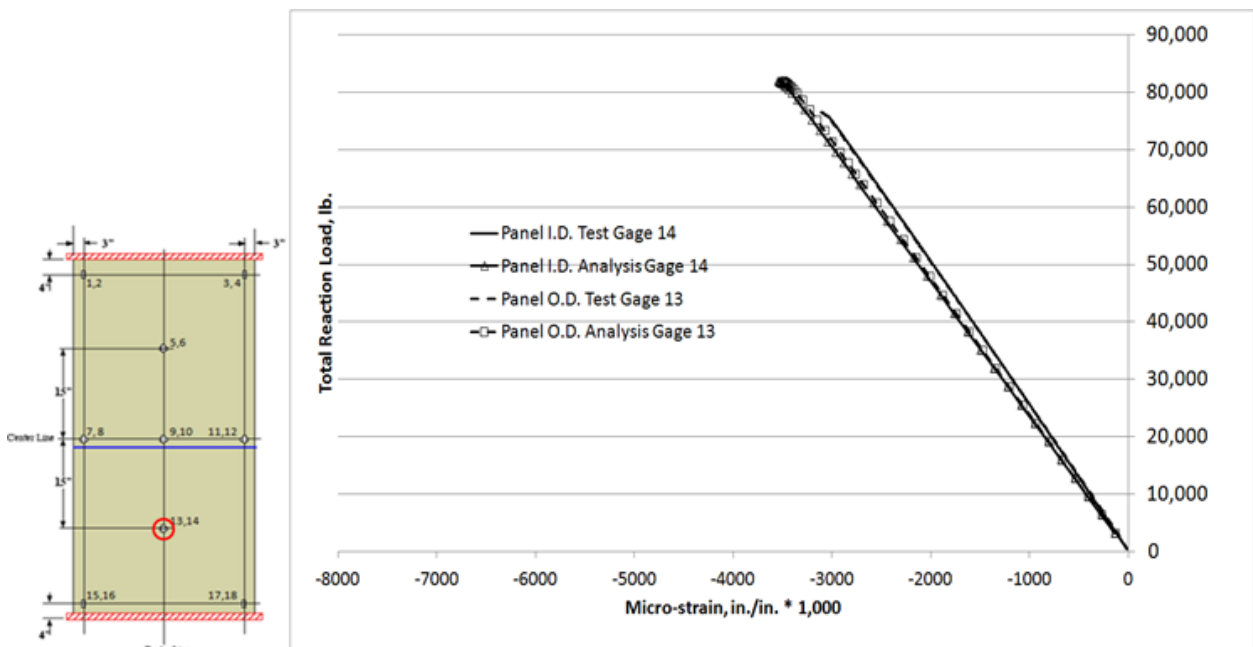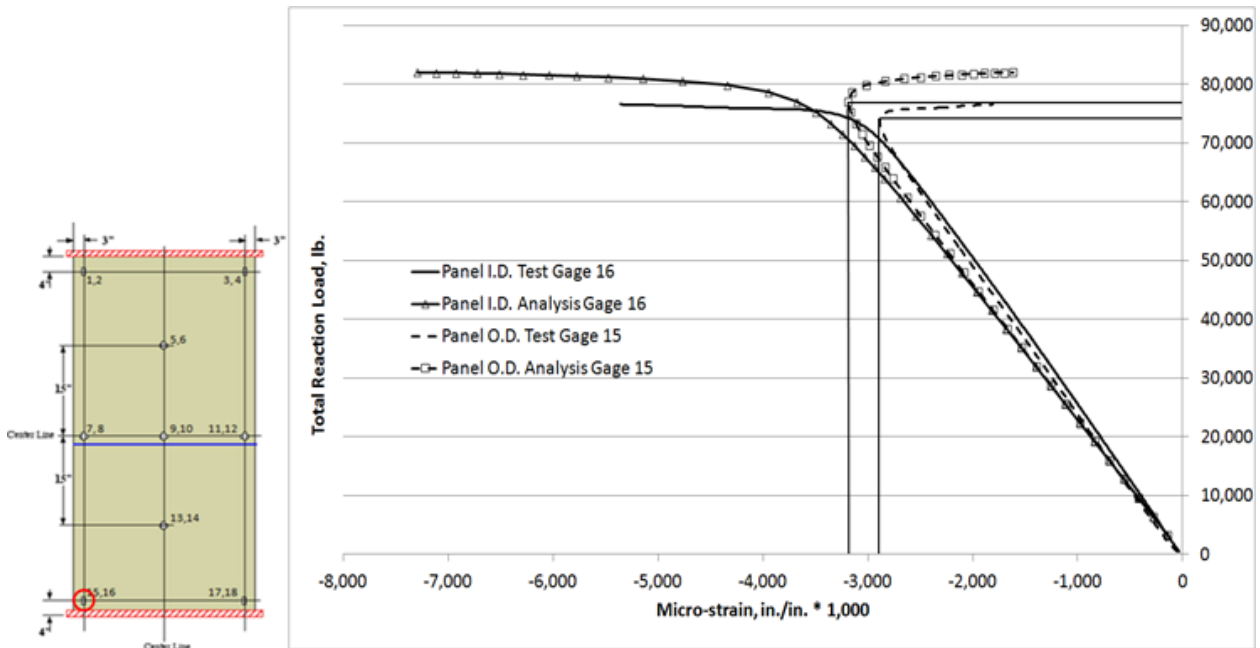

Figure 18.—Load/strain plot for gages 9 and 10, center of panel (see Figure 4). Analysis obtained from MSC/NASTRAN, Sol 106.

Figure 19.—Load/strain plot for gages 11 and 12, center of panel, right side (see Figure 4). Analysis obtained from MSC/NASTRAN, Sol 106.

Figure 20.—Load/strain plot for gages 13 and 14, centerline of panel, ¼ length (see Figure 4). Analysis obtained from MSC/NASTRAN, Sol 106.

Figure 21.—Load/strain plot for gages 15 and 16, lower left of panel (see Figure 4). Analysis obtained from MSC/NASTRAN, Sol 106.
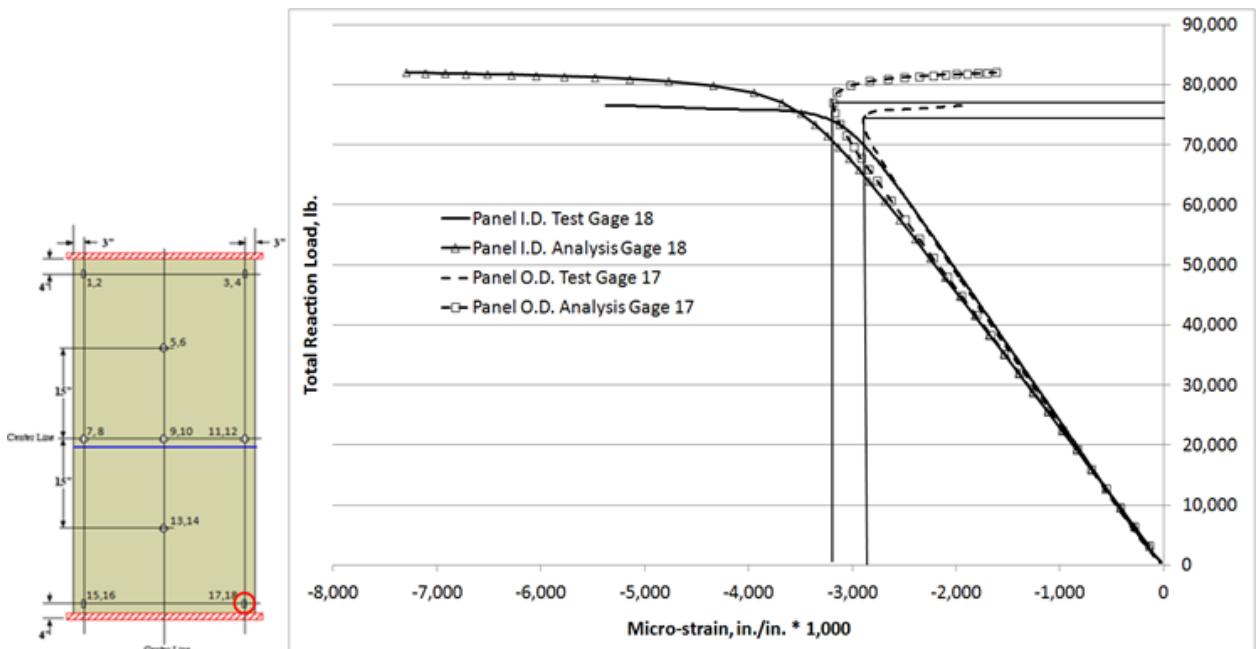

Figure 22.—Load/strain plot for gages 17and 18, lower right (see Figure 4). Analysis obtained from MSC/NASTRAN, Sol 106.

Figure 23 shows that the post-buckled, in-plane displacement photogrammetry results qualitatively compared well with the analytical predictions. Since shell elements were used in the analysis, the nodal displacements do not vary on the O.D. and I.D. surfaces, whereas, the test results showed the some slight variation in displacement for the I.D. and O.D. surfaces due to the finite width of the panel. Figure 24 shows the evolution of the in-plane displacement, obtained from the numerical analysis, as the applied compressive load is increased. Figure 25 shows that the post-buckled, out-of plane, displacement also compared well qualitatively with the analytical predictions. Figure 26 shows that the out-of-plane displacement was negligible up to the load of 77,040 lb.

For the O.D. surface, Figure 27 show that the post-buckled, minimum principal strain test results qualitatively compared well with the analytical predictions. Like the out-of-plane displacement, the minimum principal strain (compressive) was uniform up until the point of buckling, as shown in Figure 28. For the I.D. surface, Figure 29 shows that the minimum principal strain also compared well, and Figure 30 shows the predicted progression of the minimum principal strain from the analysis. Figure 31 to Figure 34 show the maximum principal strain comparison for the O.D. and I.D. Although general shapes are comparable between the analysis and test, the maximum principal strain does not compare as well as the minimum principal strain, from a qualitative standpoint. This is acceptable as the minimum principal strain was the primary strain in the buckling test. Furthermore, the magnitudes of the maximum principal strains were very low, thus slight discrepancies between the analysis and experiment are exacerbated.
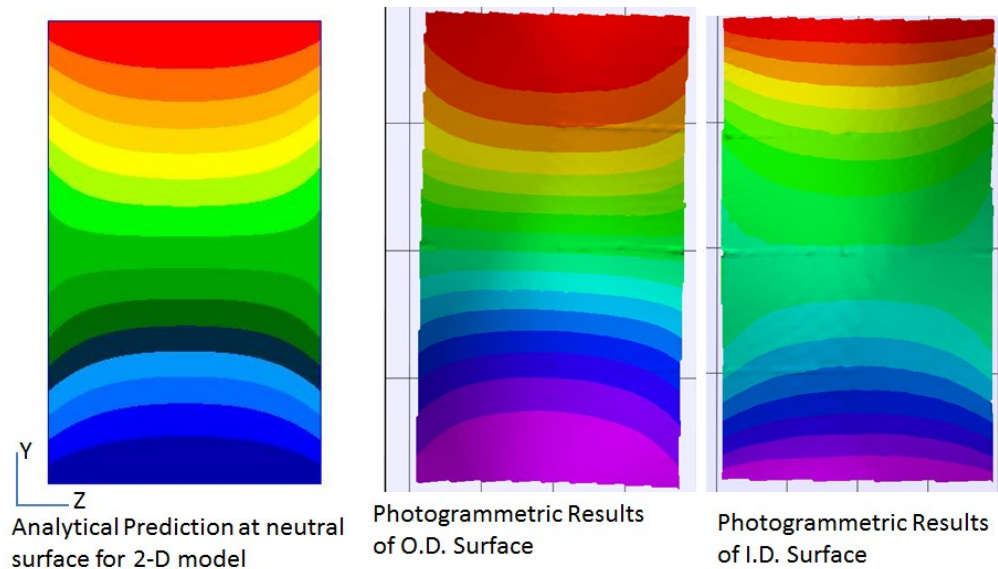

Analytical Prediction at neutral surface for 2-D model

Photogrammetric Results of O.D. Surface

Photogrammetric Results of I.D. Surface

Figure 23.—Post-buckling Y (in-plane) displacement comparison.

15,991 lb.   31,981 lb.   47,969 lb.

63,950 lb.   73,378 lb.   77,040 lb.

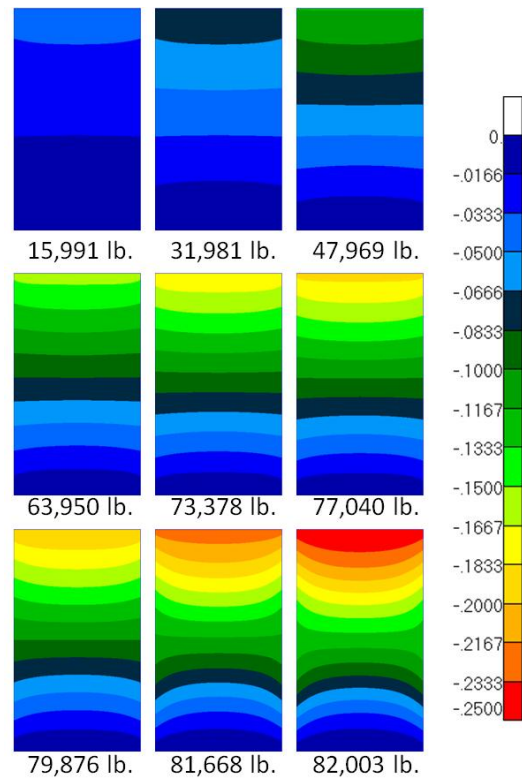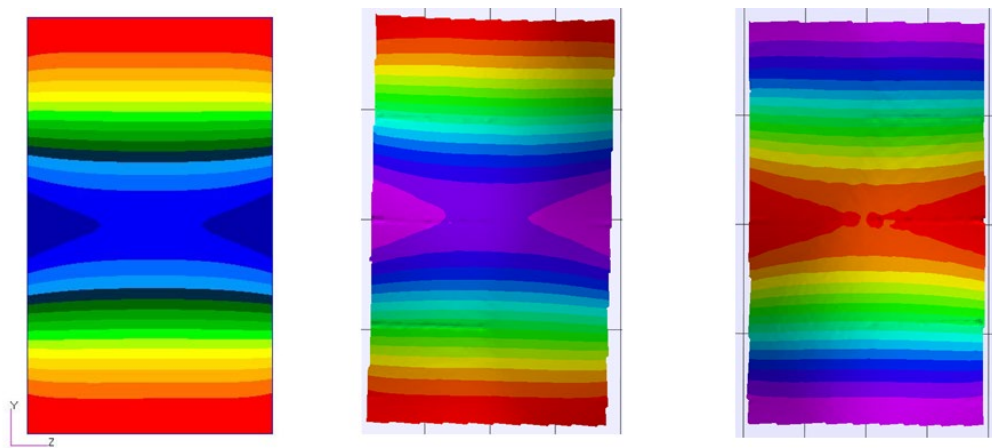79,876 lb.   81,668 lb.   82,003 lb.

Figure 24.—Analytical Y (in-plane) displacement.

Analytical Prediction at neutral surface for 2-D model

Photogrammetric Results of O.D. Surface

Photogrammetric Results of I.D. Surface

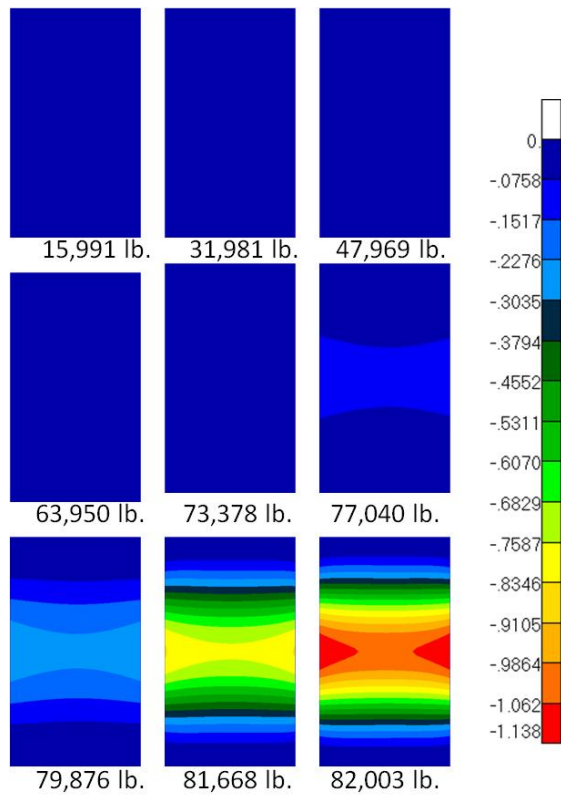Figure 25.—Post-buckling X (out-of-plane) displacement comparison .

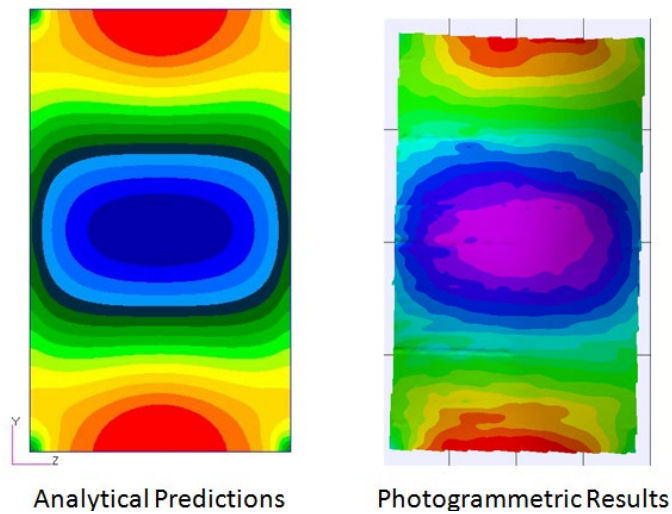Figure 26.—Analytical X (out-of-plane) displacement.

Analytical Predictions   **Photogrammetric Results**

Figure 27.—Post-buckling O.D. minimum principal (Y) strain comparison.
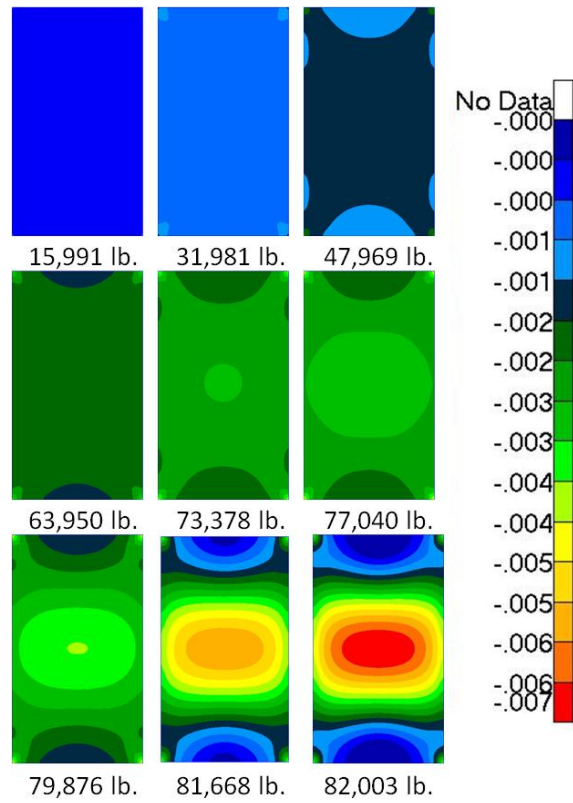
Figure 28.—Analytical minimum principal strain (Y) strain O.D.

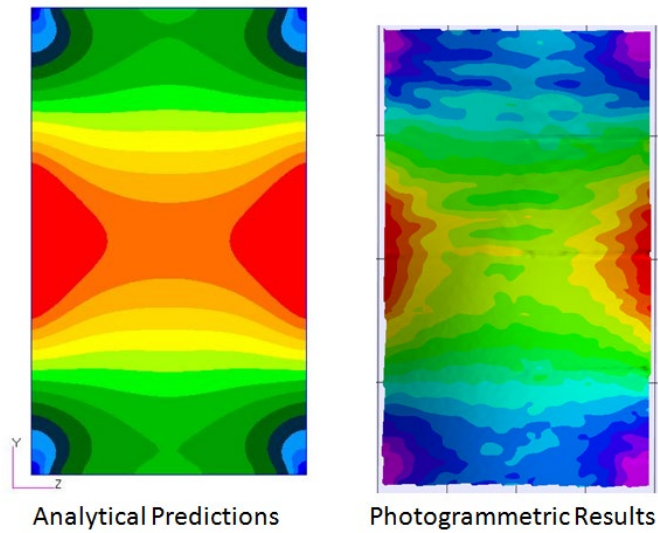Analytical Predictions   Photogrammetric Results

Figure 29.—Post-buckling I.D. minimum principle (Y) strain comparison

15,991 lb.   31,981 lb.   47,969 lb.

63,950 lb.   73,378 lb.   77,040 lb.

79,876 lb.   81,668 lb.   82,003 lb.
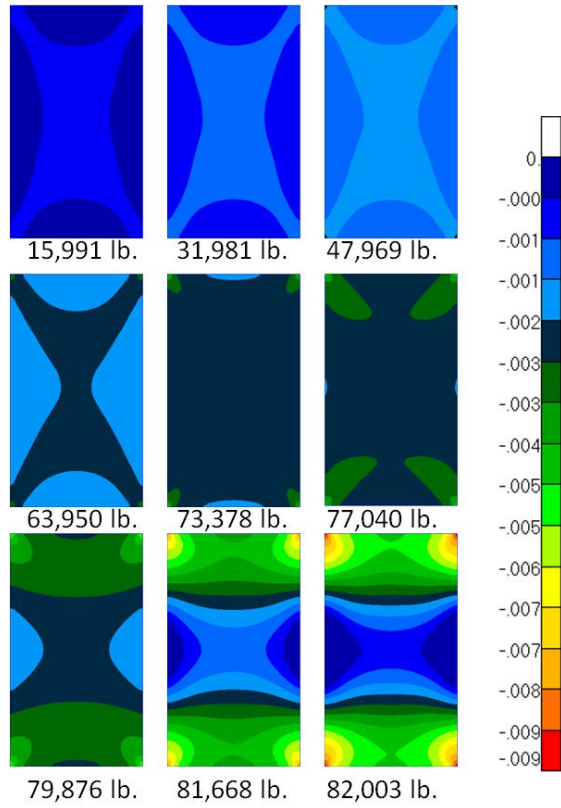
Figure 30.—Analytical minimum principle strain (Y) strain I.D.

Analytical Predictions   Photogrammetric Results
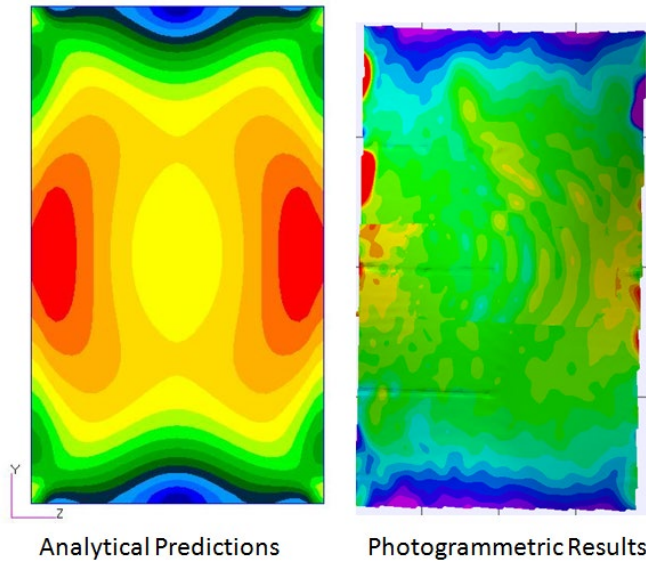
Figure 31.—Post-buckling O.D. maximum principle (Z) strain comparison.
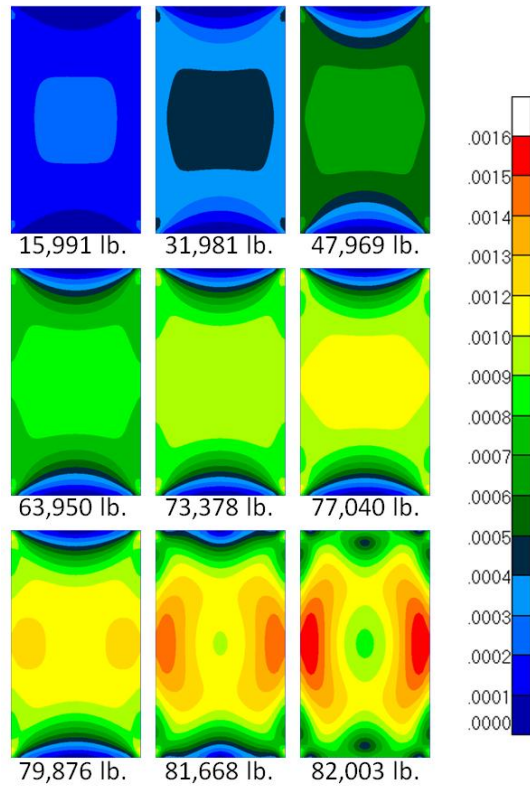
Figure 32.—Analytical maximum principle strain (Z) strain O.D.

Analytical Predictions   Photogrammetric Results
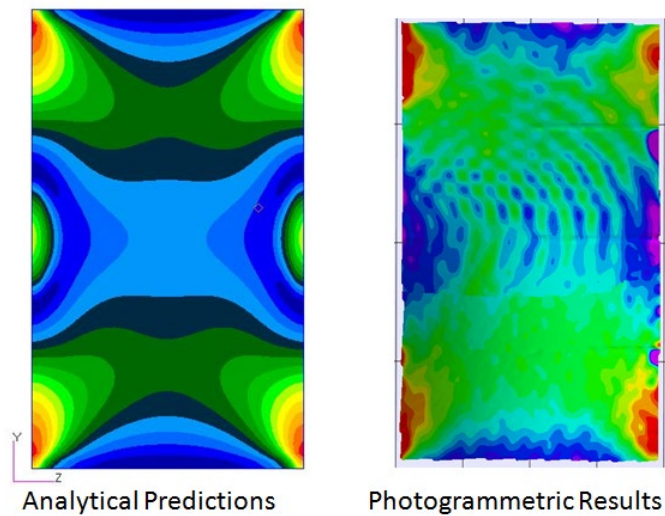
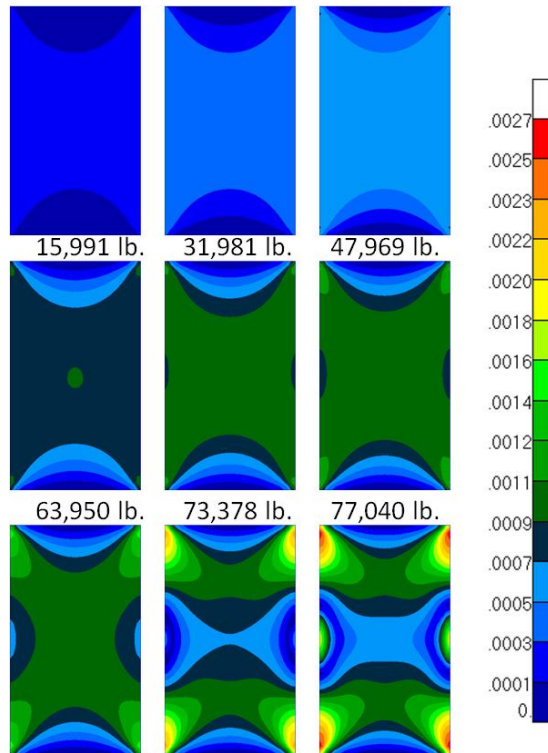Figure 33.—Post-buckling I.D. maximum principle (Z) strain comparison.

Figure 34.—Analytical maximum principle strain (Z) strain I.D.

4.3 Strength Analysis at Buckling Load

In a separate linear static analysis, the panel was loaded up to the buckling load (determined from the nonlinear static analysis) using MSC/NASTRAN Sol 101. This analysis was performed to confirm that panel failure was stiffness driven (i.e., the panel would be expected to buckle before it failed in strength). Figure 35 shows the strength ratio plot for the panel at the buckling load. The strength ratio is the local stress versus the allowable, and it incorporates one of three multiaxial failure criteria: Tsai-Wu, Tsai-Hill, Hoffman (Jones, 1999). Figure 35 shows the lowest strength ratio among the three criteria, and all facesheet plies, for each element. The analysis showed that a load 2.45 times greater than the buckling load would be required to fail the panel in strength, indicating the panel is indeed stiffness driven. It should also be noted that the regimes exhibiting the lowest strength ratios are limited to the corners of the panel, while the majority of the panel exhibits strength ratios above 3.0. The magnitude of the stresses near the corners is likely to be dependent on the size of the elements used in those areas, due to the presence of perfectly sharp corners in the model.

In addition to performing the strength analysis using MSC/NASTRAN Sol 101, a strength analysis was performed in HyperSizer, a commercially available structural sizing and design software (HyperSizer, 2012). The honeycomb properties used in this analysis are shown in Figure 36. The element forces and moments were obtained using finite element analysis and the honeycomb was constructed used explicit ply lay-ups. An element-based comparison was used to ensure that worst case behavior was captured. The following modes of failure were of most interest: core crimping, core crushing, facesheet wrinkling, and facesheet dimpling, as these modes are difficult to assess using finite element analysis alone.

Figure 37 shows that all the margins are positive for core crimping, core crushing, facesheet wrinkling, and facesheet dimpling. It should be noted that the minimum strength ratios (margin of safety plus one) from NASTRAN and HyperSizer matched very well, both indicated a strength ratio of 2.493. It was determined that the wrinkling equations used to produce the margin of safety contour plot (with a minimum margin of safety of 0.54) in Figure 38 were not appropriate for a honeycomb sandwich panel with laminated

composite facesheets (Zalewski et al., 2012). Therefore, wrinkling stress (sw) was assessed at 1.062 using the wrinkling Equation (1) for anisotropic facesheets and cellular core (Vinson, 1999), as is more appropriate for this panel. To improve the accuracy the wrinkling margin of safety, a combined loading condition was used, Equation (2), with two compressive principal stresses (Ley et al., 1999). Using this more appropriate method, the minimum margin of safety further increased from 1.062 to 2.915.

$$sw = \sqrt{\frac{2\,t_f E_c E_f}{3\,t_c(1-\upsilon_f{}^2)}} \qquad (1)$$

$$MOS = \frac{1}{\sqrt{\left(\dfrac{\sigma_1}{sw}\right)^3 + \dfrac{\sigma_2}{sw}}} - 1 \qquad (2)$$
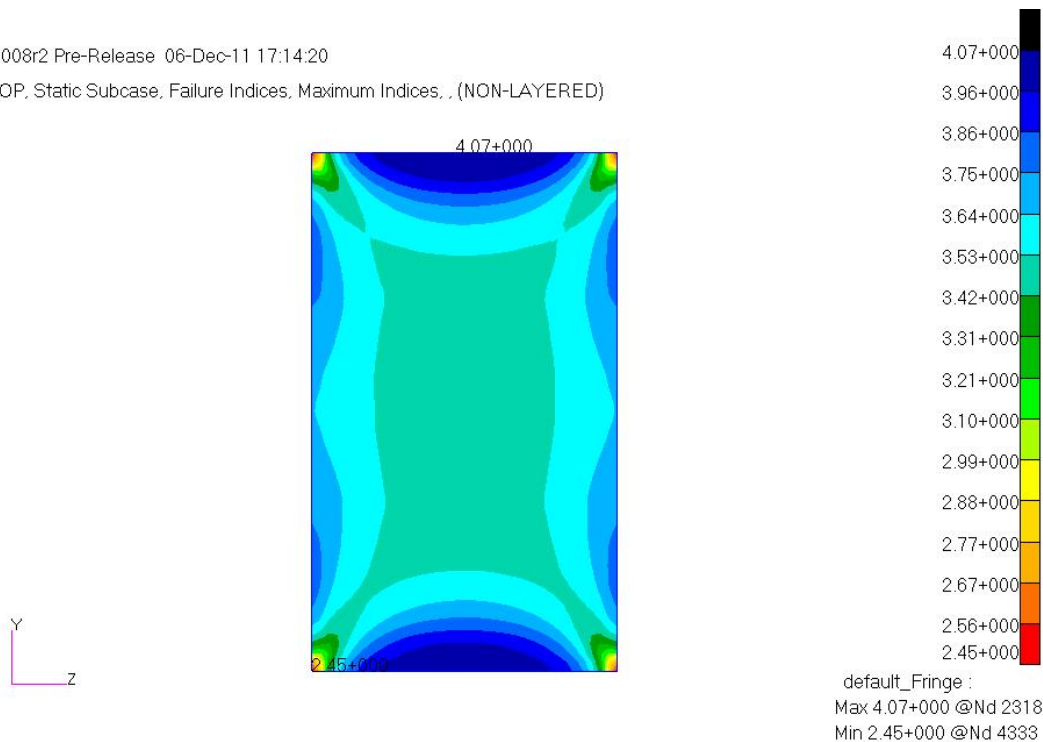
Figure 35.—Strength ratio plot at buckling load.

Figure 36.—Honeycomb Hexcel core properties.

- # Top facesheet

Limit MS	Ultimate MS	γ LS	Location - Analysis Description
1.096 (0)	1.096 (0)	1	**Top Honeycomb Face** Wrinkling, Eqn 2, Honeycomb or RCS Core, X, Y & Interaction
2.484 (0)	2.484 (0)	1	**Top Honeycomb Face** Wrinkling, Eqn 1, Isotropic or Honeycomb Core, X, Y & Interaction
19.3 (0)	19.3 (0)	1	**Top Honeycomb Face** Intracell Dimpling, X, Y & Interaction

- # Bottom facesheet

Limit MS	Ultimate MS	γ LS	Location - Analysis Description
1.062 (0)	1.062 (0)	1	**Bottom Honeycomb Face** Wrinkling, Eqn 2, Honeycomb or RCS Core, X, Y & Interaction
2.426 (0)	2.426 (0)	1	**Bottom Honeycomb Face** Wrinkling, Eqn 1, Isotropic or Honeycomb Core, X, Y & Interaction
18.97 (0)	18.97 (0)	1	**Bottom Honeycomb Face** Intracell Dimpling, X, Y & Interaction

- # Core

Limit MS	Ultimate MS	γ LS	Location - Analysis Description
12.82 (0)	12.82 (0)	1	**Honeycomb Core** Shear Crimping, Min X, Y (Hexcel)
Very High	Very High	1	**Honeycomb Core** Crushing, Flexural Bending Load

- # Tsai-Wu

Ultimate MS	γ LS	Location - Analysis Description
1.493 (0)	1	**Bottom Honeycomb Face** Composite Strength, Tsai-Wu Interaction

- # Strength Ratio (NX Nastran)= 2.4934
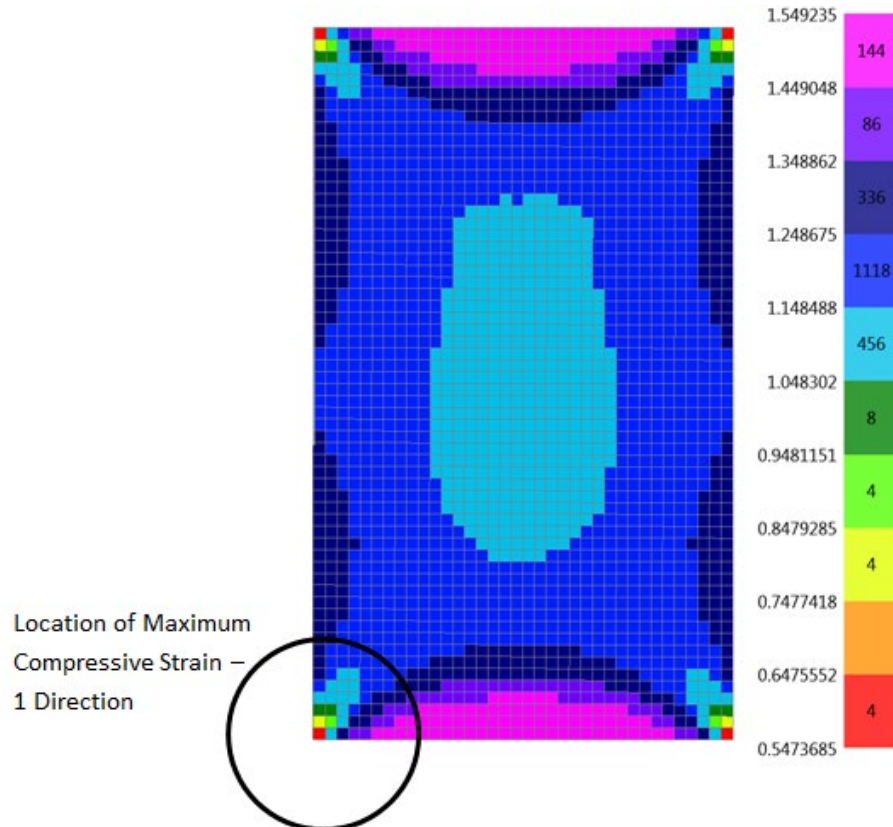
Figure 37.—HyperSizer results.

Figure 38.—HyperSizer margin of safety plot for core crimping, core crushing, facesheet wrinkling, and facesheet dimpling.

5.0   Sensitivity Studies

5.1   Sensitivity to Panel Geometry

The analysis presented in Section 4.2 utilized geometric imperfection data from the panel measured vertically along a single horizontal coordinate. It is very likely, that if a different location was chosen to measure this data, the bow shape, and maximum imperfection would have been different. To determine the sensitivity of the panel response to variations in this bow shape, a parametric study was conducted incorporating various levels of bow imperfection. MSC/NASTRAN, Sol 106 was used for the FEM analysis. The bow was introduced into the panel geometry as an arc, and the maximum deflection of that arc was varied: 0.01500, 0.01600, 0.01700, 0.02000, and 0.03000 in. towards the I.D. Figure 39 and Figure 40 show the sensitivity of the initial panel bow geometry on overall panel response. The results show that the stiffness was not affected by changes to the magnitude of the bow, unlike the post-buckling load. In addition to the buckling load, the buckling direction is influenced by the magnitude of the bow. For relatively small bow shape (0.01500 to 0.01600 in.) the bow buckles outward towards the major curvature in the panel. However, if the magnitude of the bow exceeds 0.01700 in. toward the I.D., the panel buckles inward, away from the major curvature. As the bow is increased from 0.01500 in. to 0.01700 in. the buckling load also increases because the direction of the imperfections is opposite the natural buckling direction and offers some slight, additional resistance. The maximum buckling load is obtained when the magnitude of the bow (0.01700 in.) is just enough to drive the panel to buckle towards the I.D. Additional imperfections beyond 0.01700 in. are henceforth aligned with the buckling direction and serve to promote buckling at earlier loads.
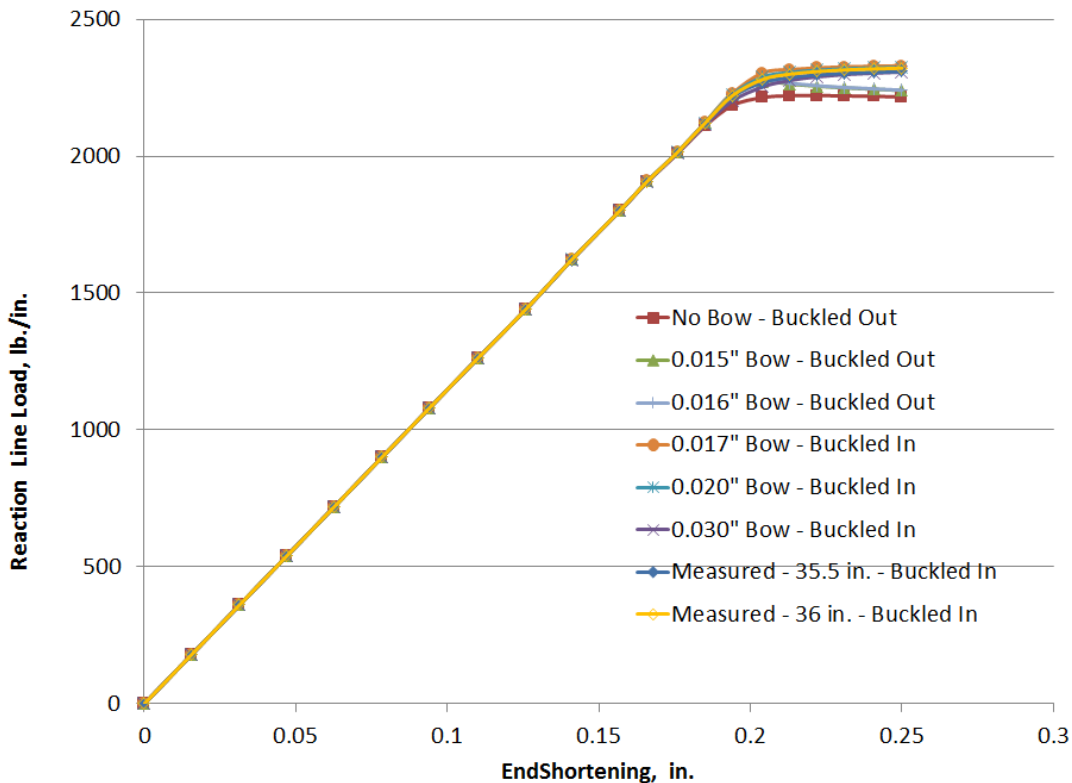

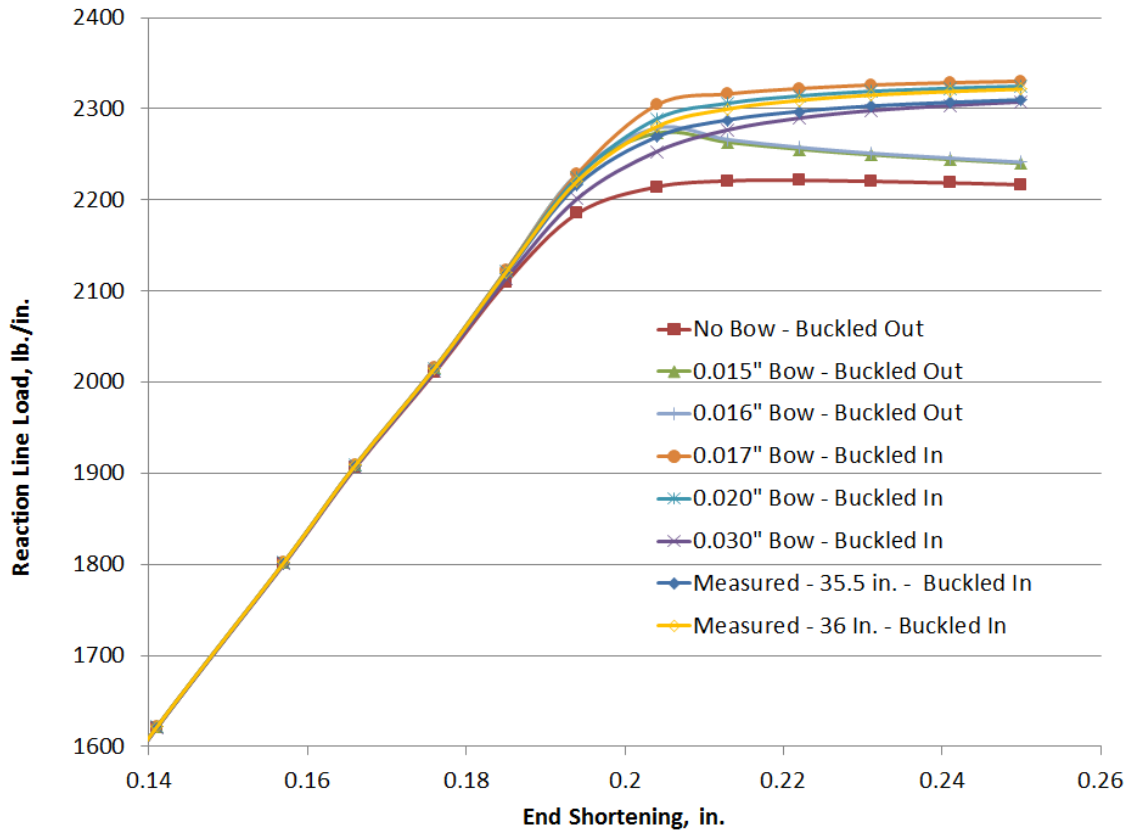Figure 39.—Impact of initial panel bow geometry on panel stiffness.

Figure 40.—Impact of initial panel bow geometry on panel stiffness (magnified view).

In addition, the panel with a 36.00 in. arc width was compared with a panel with a 35.50 in. arc length (width of the test panel). Figure 40 does not show an appreciable difference between the line-load versus end shortening response of the two different panel sizes. However, these changes are more noticeable when the total reaction load versus end shortening is observed. Thus, it is important to have accurate measurements of the panel geometry to obtain accurate buckling load predictions.

5.2   45° Ply Fiber Misalignment Sensitivity Study

To determine the sensitivity of the panel response to additional imperfections that may be introduced during the manufacturing process, several MSC/NASTRAN Sol 106 analyses were performed in which the orientation of the 45° plies were perturbed from 45° to 46°, 46.5°, 47°, 48°, 49° and 50°. Figure 41 and Figure 42 indicate that both panel stiffness and buckling load can be moderately affected by these fiber misalignments. Additionally, the stiffness of the panel with 46.5° plies (a viable scenario with the test article) corresponds best with the test article stiffness. The 0° and 90° plies were not altered as it was assumed that their orientations do not vary during the ply lay-up process.

This parametric study shows that ply angle orientation affects the analysis results such that they envelope the test results. The chosen ply orientations represent the worst case situation as the angle may not be constant but variable throughout the panel (possible larger angle deviations in the middle or edge of panel). A fiber placement or draping simulation would better model the true fiber alignment. However, the present study can be used to bound the results of the simulation when fiber misalignment is suspected as an influencing factor. From Figure 41 the slight 1.5° variation, to 46.5°, shows a very good match with the measured stiffness.
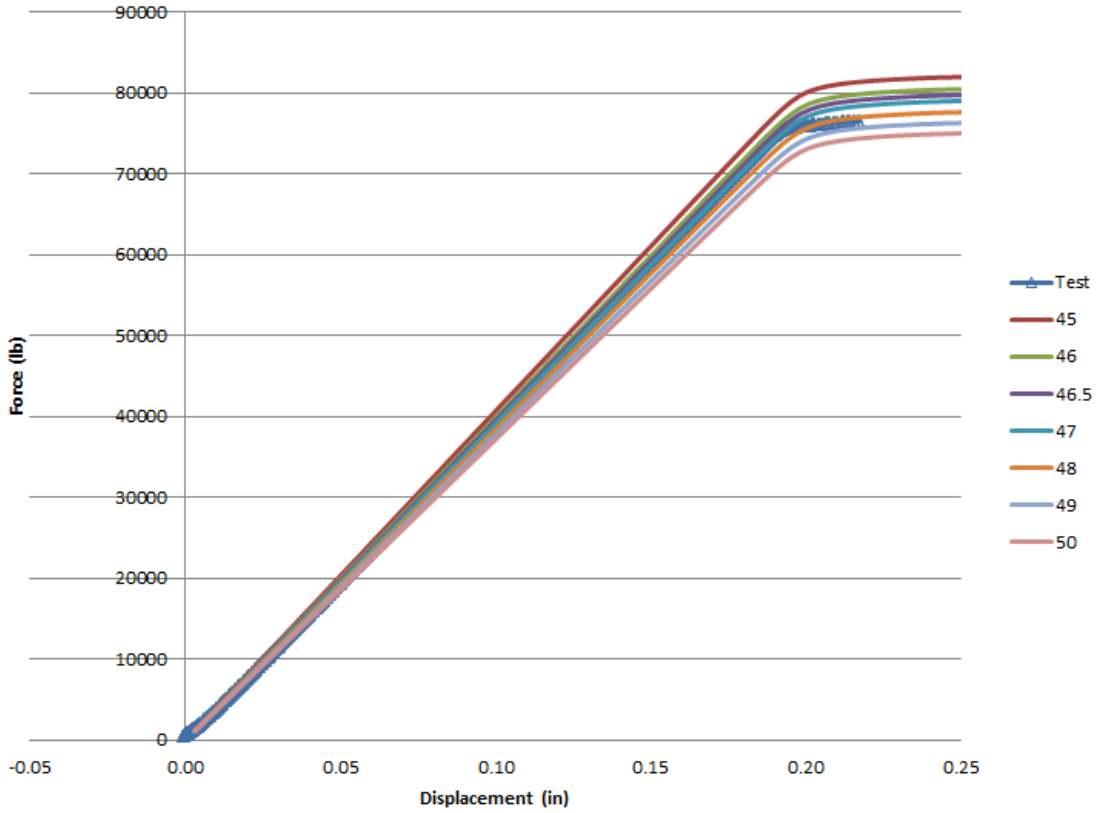
Figure 41.—Nonlinear static analysis results for altered 45° ply angle compared with test results.
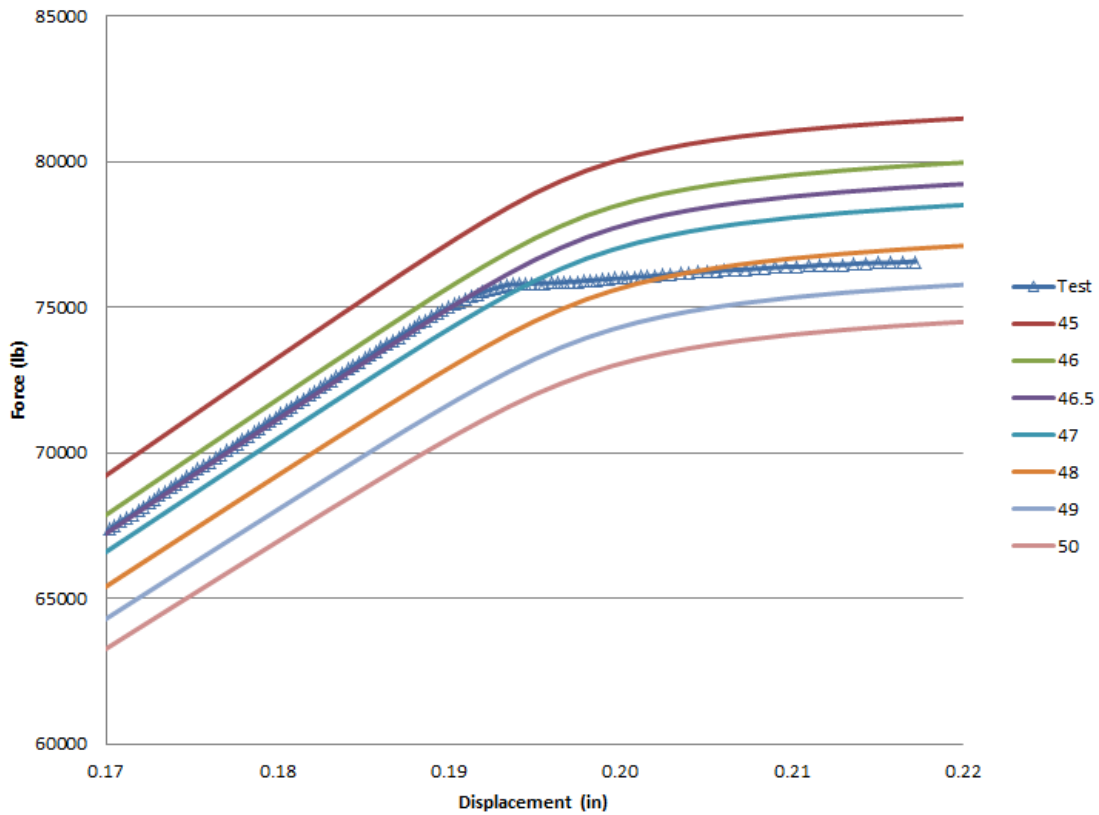

Figure 42.—Nonlinear static analysis results for altered 45° ply angle compared with test results (magnified view).

5.3   ANSYS Three-Dimensional (3–D) Finite Element Model

The 3- by 5-ft arc segment sandwich panel was investigated using two different ANSYS finite element models. The first model was a 2–D layered structural shell element from which the results have been presented earlier. The second model was a 3–D layered structural solid-shell element model in which the test fixturing was also included. In ANSYS, the 2–D layered shell element is called a SHELL281 finite element, and the 3–D solid-shell is called a SOLSH190 finite element. These finite element types are shown in Figure 43. A shell element is similar to a NASTRAN quad element, while the solid-shell is similar to a brick element. The SOLSH190 element can be used to model shell structures with a wide range of thickness from thin to moderately thick. Furthermore, the SOLSH190 element formulation permits small thickness to length ratios without producing errors due to large aspect ratios. The thickness between the nodes must equal the sum of the individual layer thicknesses. Otherwise, ANSYS will scale the individual layer thicknesses to fit the actual element thickness. Since the results of the 2–D shell model were included with the ABAQUS and MSC-NASTRAN results in previous sections, these results will only be used as a basis of comparison with the 3–D finite element model.

Figure 44 shows the model of the test panel geometry with the end plates. For clarity, the finite element edges are suppressed. The panel was modeled as 62 in. tall including the 1.000 in. Al end plates and 36.00 in. wide along the chord. The top and bottom 1 in. portions of the panel were supported in the potting material and end plates. Figure 45 shows the slot in the end plate shaped like the arc segment test specimen model. The end of the specimen model is centered in the slot, and the 0.5000 in. space around the specimen is filled with solid elements modeling the UNISORB V-100 potting compound with the elastic properties given in Table VI. Each color represents a different material assignment: cyan for the IM7/977-3 facesheets, purple for the honeycomb core, red for the potting compound, and orange for the Al end plates.

SHELL281

2-D 8-Node Structural Shell
with Layered Composite Capability

SOLSH190

3-D 8-Node Structural Solid Shell
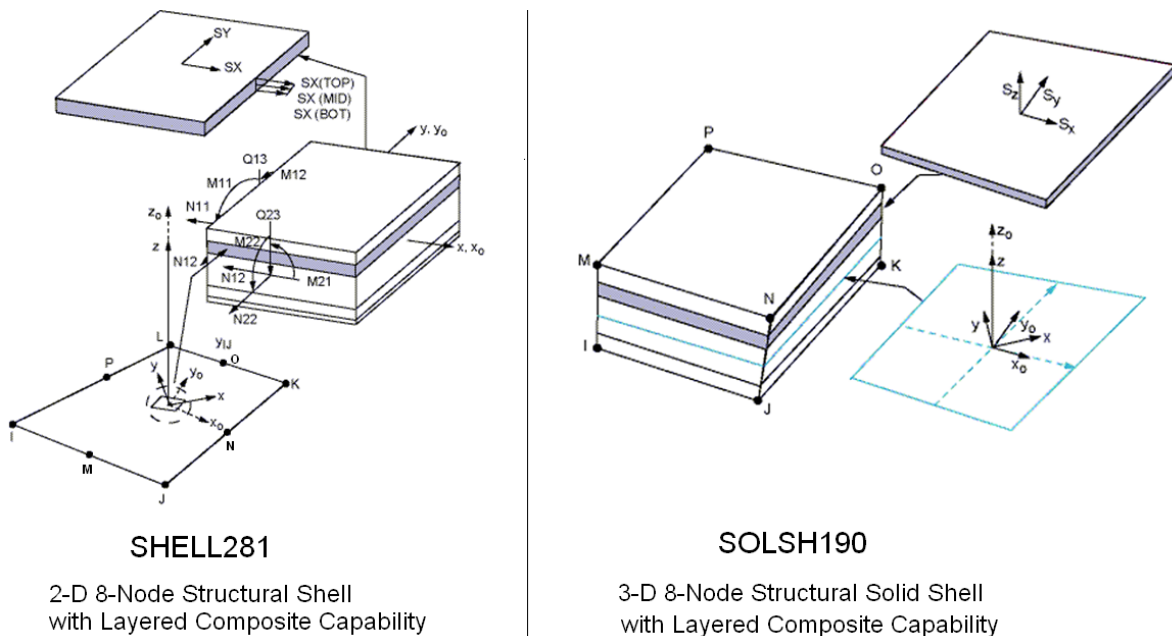with Layered Composite Capability

Figure 43.—ANSYS 2–D shell versus 3–D solid-shell (brick) finite elements.

TABLE VI.—ELASTIC PROPERTIES FOR
UNISORB V-100 POTTING COMPOUND

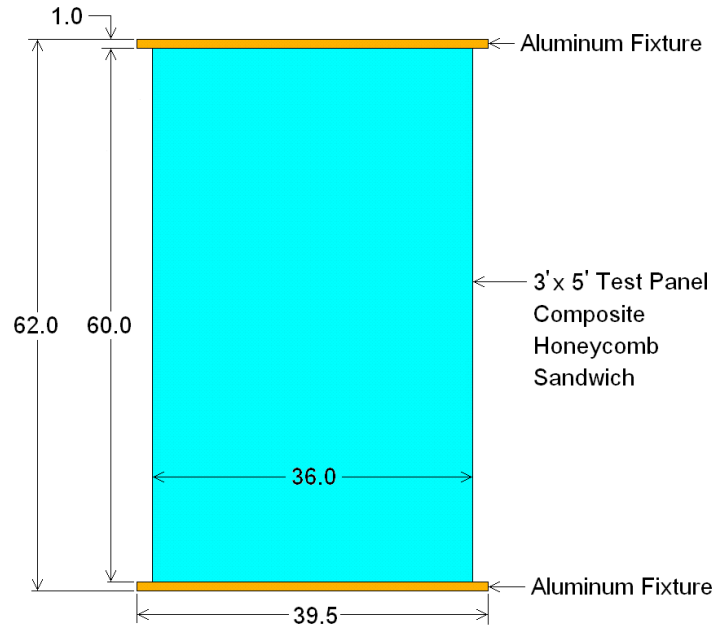| Property	Value
E	436 ksi
ν	0.35

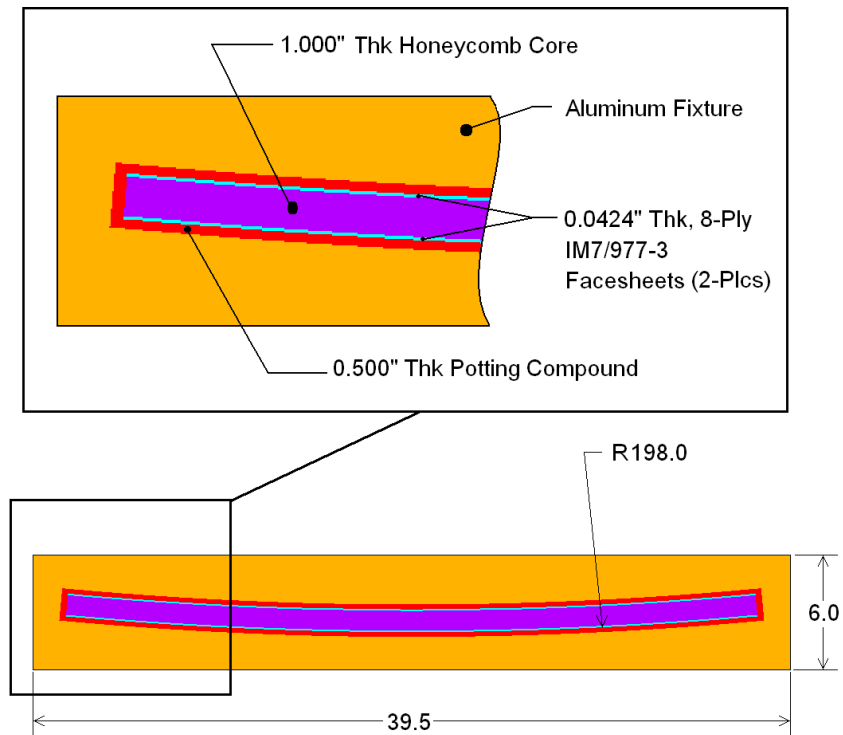Figure 44.—The 3- by 5-ft arc segment test panel configuration.

Figure 45.—The 3- by 5-ft arc segment test panel and test fixture end view.

The solid model was generated using a script file containing ANSYS preprocessing, finite element solution, and post-processing commands in the ANSYS Parametric Design Language (APDL) (ANSYS, 2011). The basic geometry, ply stacking sequence, material properties, and geometric imperfections were defined using parameters. The script file can generate the finite element model, perform each analysis in sequence, and process the results in tabular or graphic format.

As shown in Figure 46, the stacking sequence of the facesheets was $[45°/90°/–45°/0°]_S$ with 0.005300 in. thick plies. Again, the IM7/977-3 elastic properties and allowables were obtained from Orion materials database, and they are not listed due to ITAR restrictions (Lockheed Martin, 2010). Referring to Table VII, the Al (5052-T6 alloy) honeycomb properties were obtained from commercially available literature (Alcore). Unlike the HyperSizer properties, the honeycomb in-plane longitudinal and transverse moduli (E_1 and E_2) were kept at 21.28 psi, and the in-plane shear modulus (G_{12}) was kept at 5.32 psi in the ANSYS models. The honeycomb normal (out-of-plane) modulus (E_3) was also kept at 75 ksi.
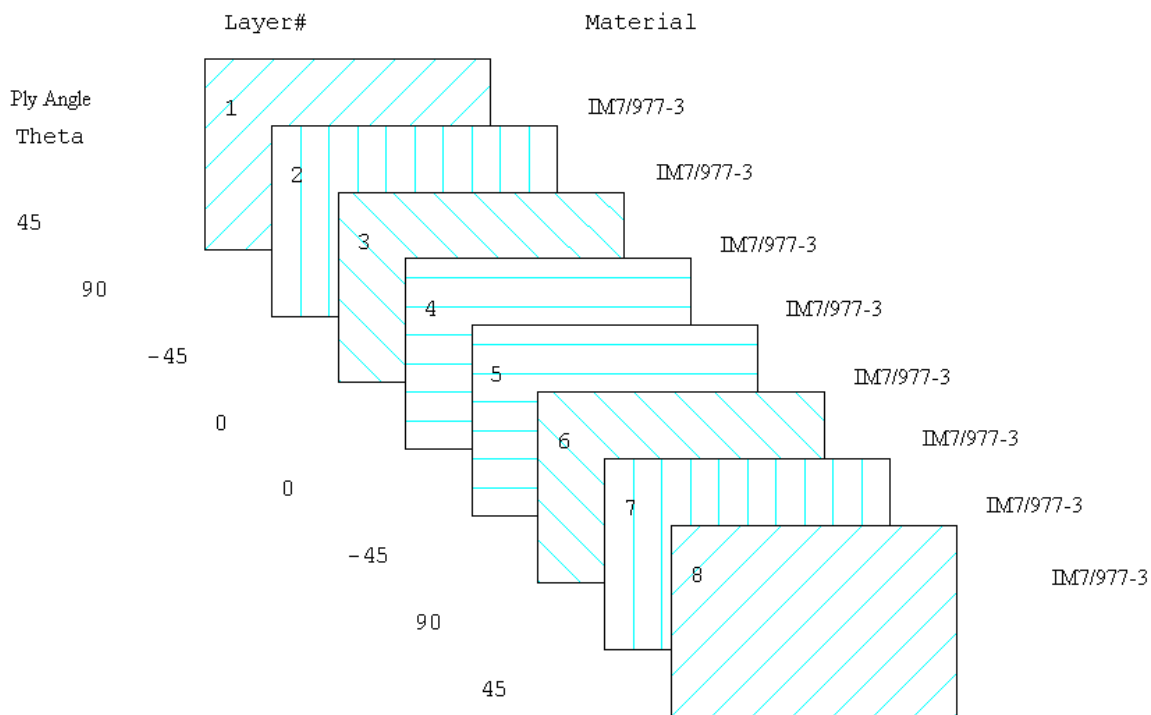
Figure 46.—Facesheet 8-ply stacking sequence.

TABLE VII.—ANSYS MODEL, Al HONEYCOMB MATERIAL
PROPERTIES, 3.1 pcf, 1/8-in.-5052-0.0007-in. THICKNESS

Property/units	Value	Property/units	Value
E_1, psi	21.28	ρ, pcf	3.1
E_2, psi	21.28	F_{t1}, psi	215
E_3, ksi	75	F_{c1}, psi	215
υ_{12}	0.333	F_{t2}, psi	215
υ_{23}	1.0×10^{-5}	F_{c2}, psi	215
υ_{13}	1.0×10^{-5}	F_{t3}, psi	130
G_{12}, psi	5.32	F_{c3}, psi	300
G_{13}, ksi	45	F_{s12}, psi	90
G_{23}, ksi	22	F_{s23}, psi	90
γ, lb/in^3	0.00179	F_{s13}, psi	90

Figure 47.—ANSYS solid model boundary conditions.

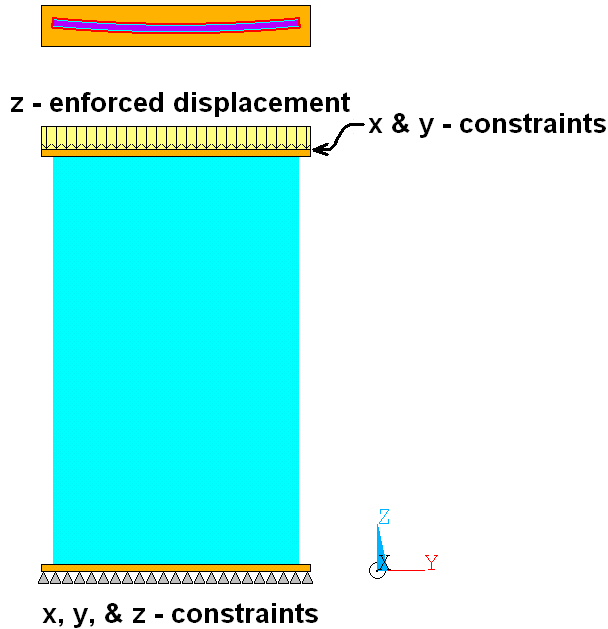The actual panel was secured between two loading platens, with the bottom end plate fixed on the loading platen. The top end plate moved with the top platen in the axial direction. Referring to Figure 47, all three displacements in the solid-shell finite element model were fixed along the bottom edge of the panel and end plate. The same boundary condition was applied to the top panel edge and top end plate, except a displacement was applied in the negative z-axis direction.

It has been shown in this paper that the initial geometric imperfections have an impact on the buckling load and direction. Intuitively, a curved panel is expected to buckle towards the O.D. However, this 3- by 5-ft arc segment test panel buckled toward the I.D., which was primarily due to its bowed shape. Therefore, the initial imperfect geometry is important in a nonlinear buckling analysis (Hong and Jun, 1989). If the 3- by 5-ft panel is modeled as perfectly symmetric (i.e., in geometry and loading), nonlinear progressive collapse does not occur numerically in ANSYS.

One way to introduce anti-symmetry to the model is to apply small perturbations to the applied loads or enforced displacements. This method is not ideal, because it is difficult to determine how to redistribute the loads. Furthermore, varying the load across the top of the panel too drastically could change the problem completely. Another way to introduce anti-symmetry is to superimpose small geometric imperfections (similar to those caused by manufacturing) on the model to trigger the buckling responses. One way to generate these imperfections is with pseudo-random shapes, where the coordinates of the nodes are slightly modified with random amplitudes. The disadvantage in using random imperfections is that they cannot be repeated, and the results would differ for each analysis of the same panel. An easier way to impose geometric imperfections on the finite element model is to employ the linear (Eigen) buckling mode shapes.

The buckling analysis of the 3- by 5-ft arc-segment panel requires several steps. First, the initial bow shape is imposed across the width of the panel model. The imperfections are obtained by running a preliminary linear buckling analysis, then updating the geometry of the finite element model to the deformed configuration. This technique is done by adding the displacements from the mode shapes multiplied by a scaling factor. The scaling factor is on the order of the manufacturing tolerances and initial bowed shape. A factor of –0.02000 in. was chosen for the 3- by 5-ft panel. Furthermore, the scaling factor was negative to correspond to the direction of the initial bow shape. Applying a positive value could bring the panel model back to a near perfect condition. The imperfections are also added as a sum of the first 10 modes shapes extracted in the preliminary linear buckling analysis as shown in Figure 48. The first 10 mode shapes were used to avoid any bias in the imperfections. Figure 49 shows the resulting geometry.

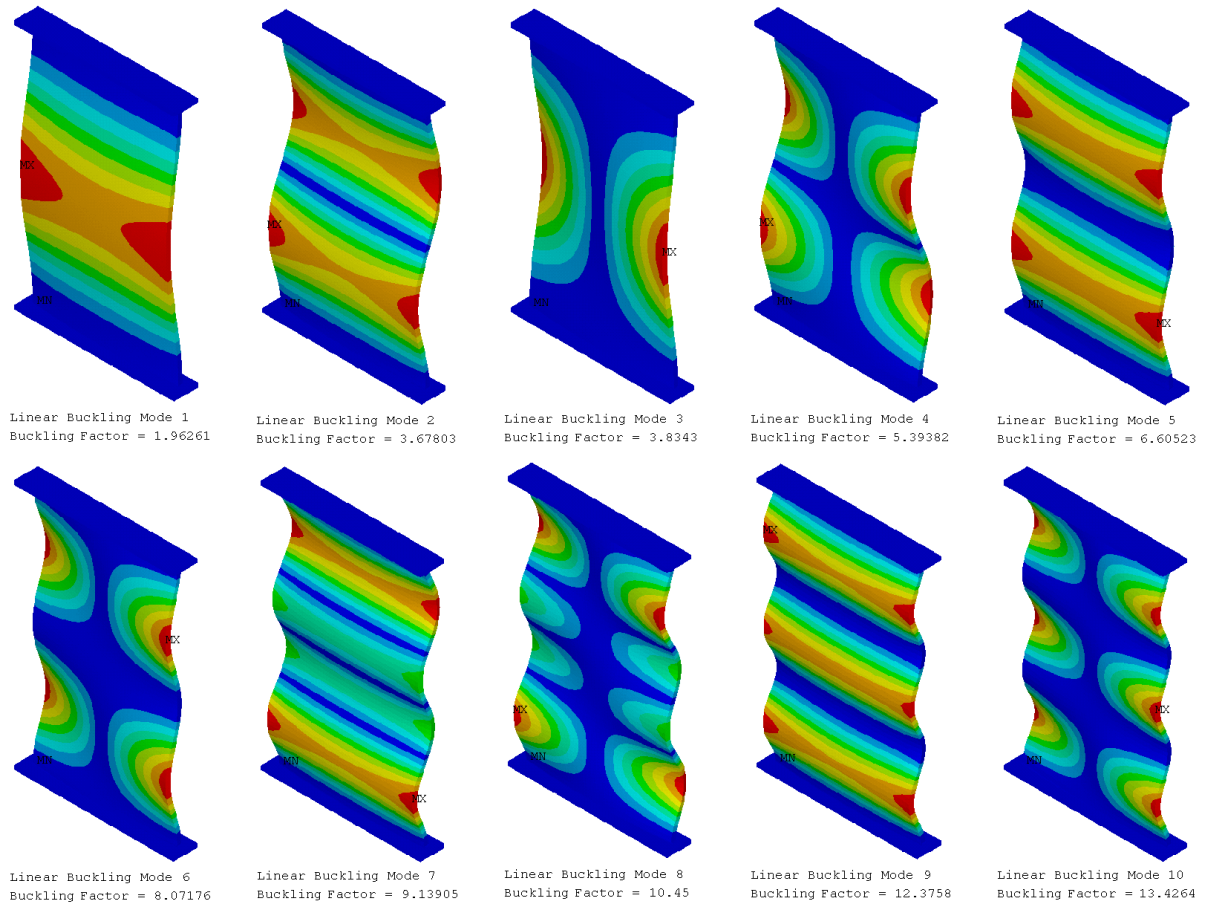Figure 48.—The first 10 linear buckling mode shapes for the 3- by 5-ft (8000-CMDP) panel.

Perfect Geometry
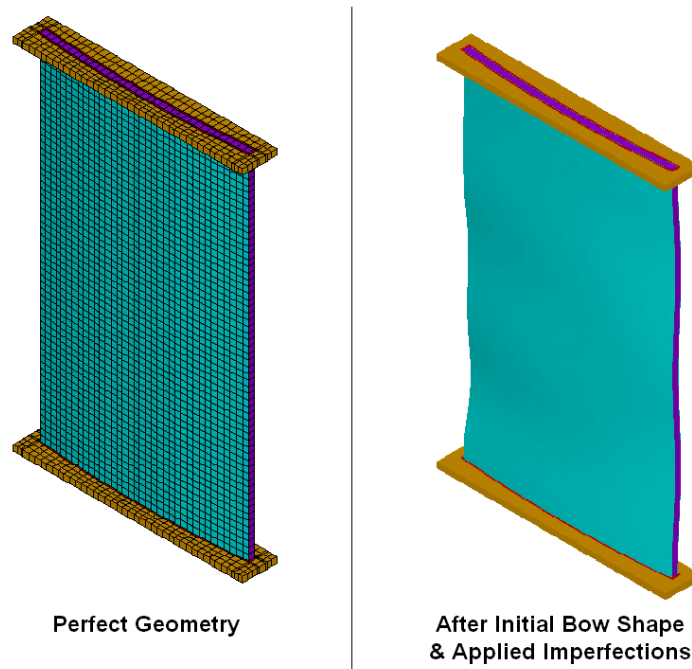
After Initial Bow Shape & Applied Imperfections

Figure 49.—Panel model with the applied initial bowed shape and geometric imperfections (exaggerated).

After the geometric imperfections are added to the finite element model, the nonlinear buckling analysis is performed. In ANSYS, a nonlinear buckling analysis is a static analysis with large deflections active. The magnitude of the applied axial compression is extended beyond the first linear (Eigen) buckling mode. In this analysis the compression was increased gradually using small time increments to predict the critical buckling load.

Figure 50 shows the reaction load versus end compression for the linear and nonlinear shell and solid ANSYS models and the actual test data. All four analyses over-predicted the buckling load, but the nonlinear solid FEM is closest to the test result buckling load. In both nonlinear ANSYS analyses, the panel stiffness was nearly the same. However, the predicted stiffnesses were higher than the test stiffness. Reasons for the difference in stiffness were discussed earlier.

Figure 51 shows the panel radial displacement plot (radial component of the total displacement field) when –0.2270 in. was applied to the edge. As explained earlier, Figure 51 shows that the panel buckles inwards towards the I.D. due to the initial bow and not in the direction of the panel's outer surface.

Figure 52 to Figure 54 show load versus strain plots for gages located in the vertical center of the panel for the solid element model. On the I.D. side of the panel, the strain goes into compression up to buckling, and then strain is relieved as the load increases during post-buckling as it goes toward tension. On the O.D. side, the strain remains compressive (negative) and suddenly increases in magnitude during post-buckling. The analysis results for the ANSYS solid FEM show the same trends as the actual strain gage data.
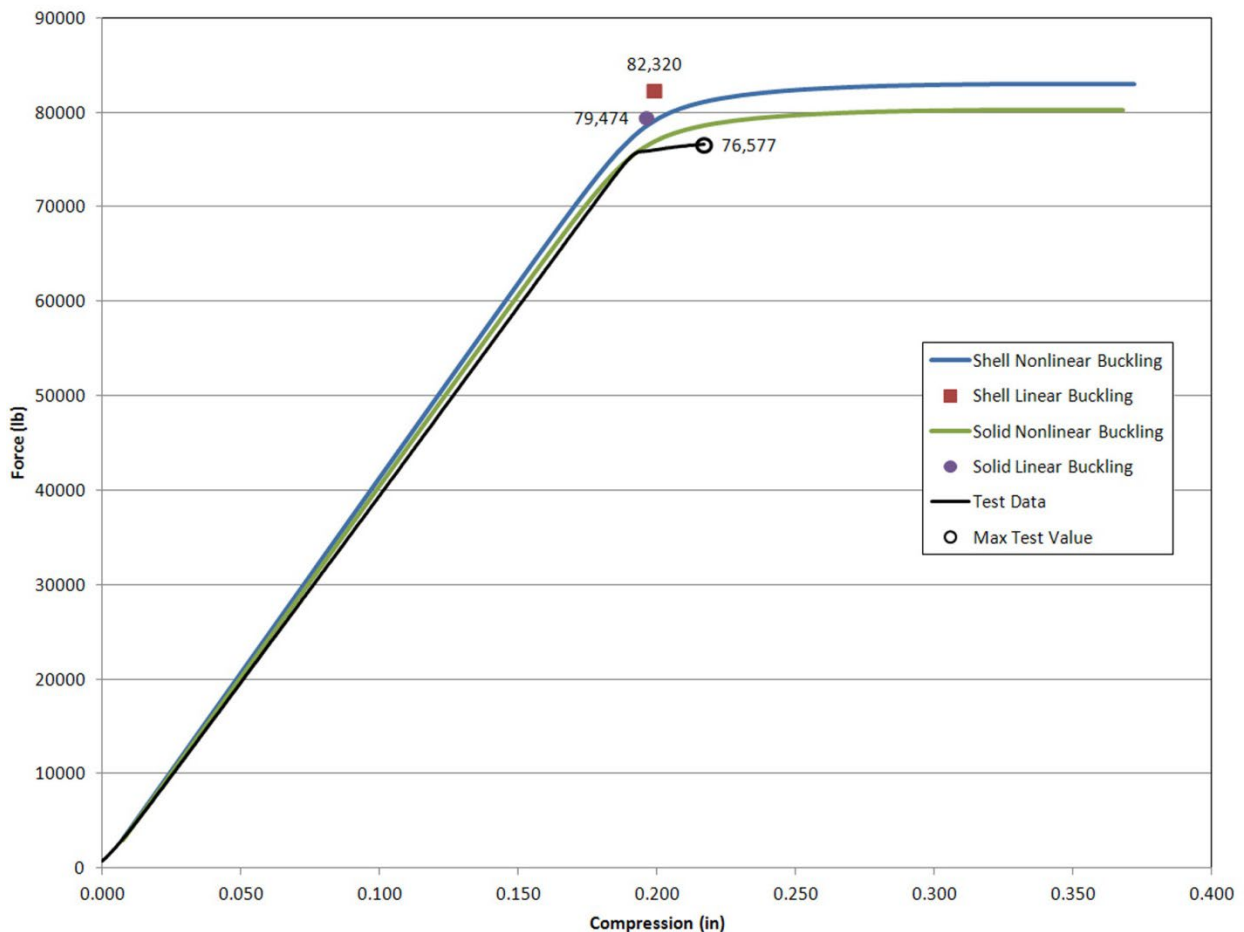
Figure 50.—Total reaction load versus end shortening for ANSYS solid and shell FEM's.
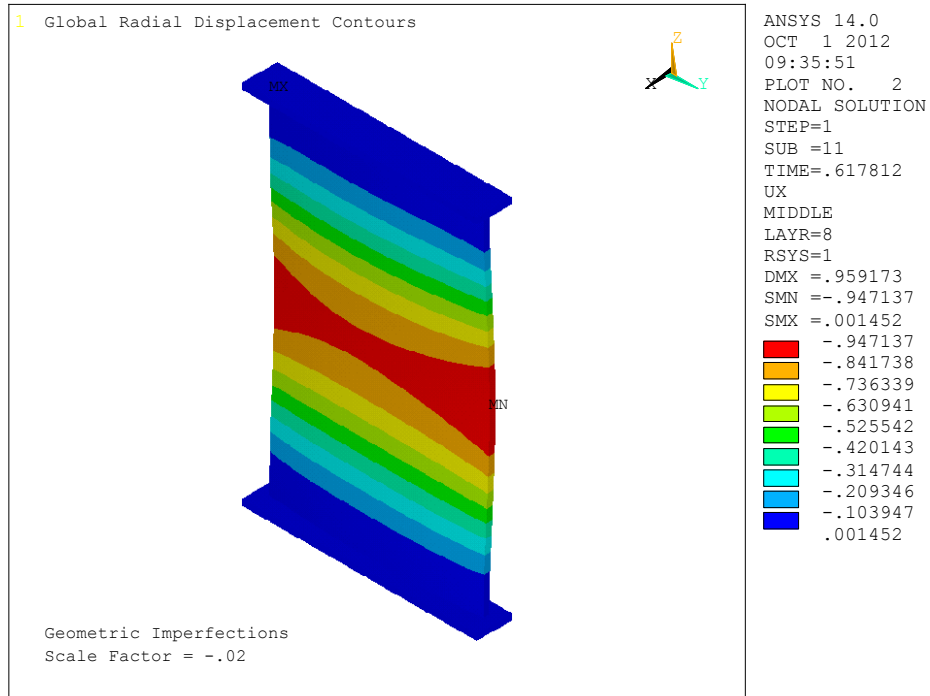
Figure 51.—ANSYS solid FEM, radial displacement contour plot at 0.227-in. end shortening.
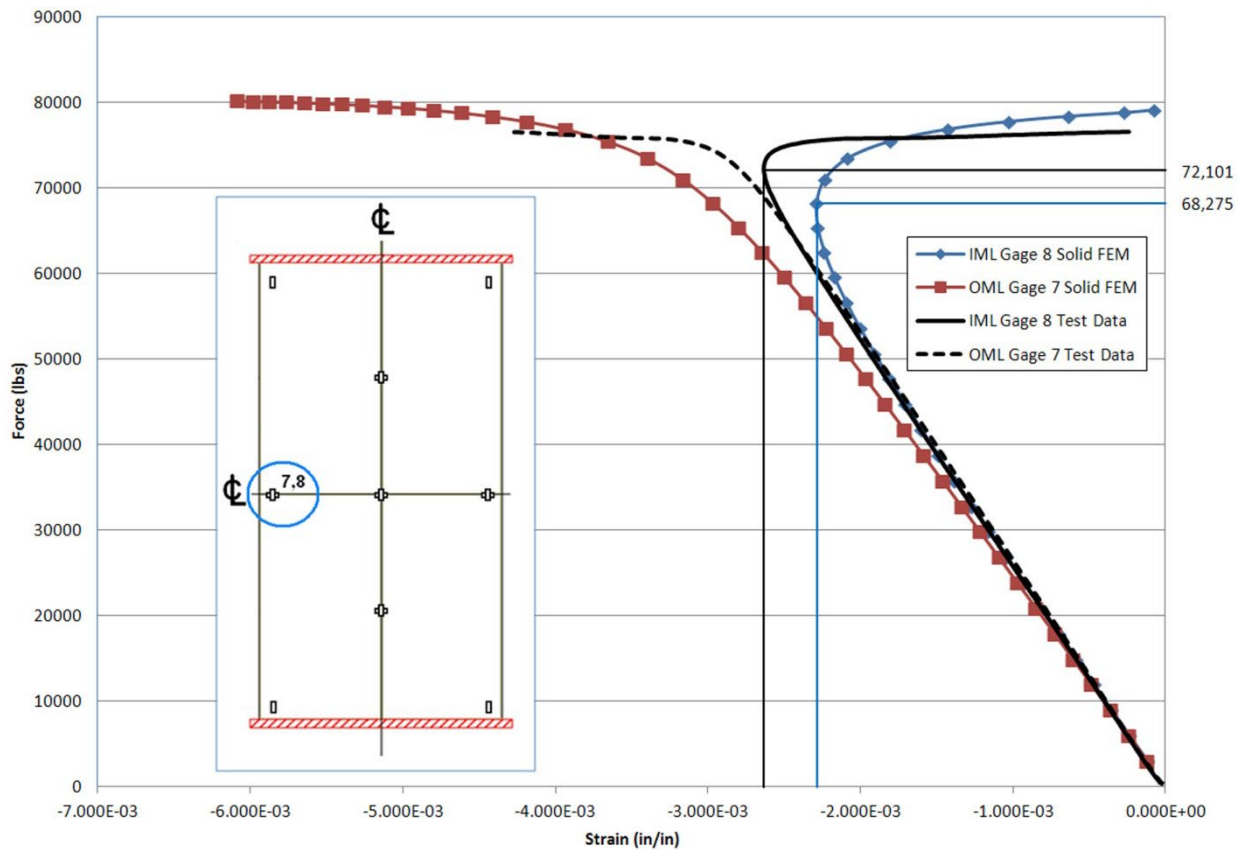
Figure 52.—Load versus minimum principal strain plot for gages 7 and 8 (see Figure 4).

Figure 53.—Load versus minimum principal strain plot for gages 9 and 10 (see Figure 4).

Figure 54.—Load versus minimum principal strain plot for gages 11 and 12 (see Figure 4).

6.0 Conclusion

Experimental and analytical results have been presented pertaining to the buckling of a 3- by 5-ft, curved, sandwich panel: Panel A (see Table I). The panel was composed of a 1.000 in. thick Al honeycomb core and 8-ply, quasi-isotropic, in-autoclave cured, IM7/977-3, laminated composite facesheets cut from a 1/16th arc segment of a 10.0 m barrel. Experimental and model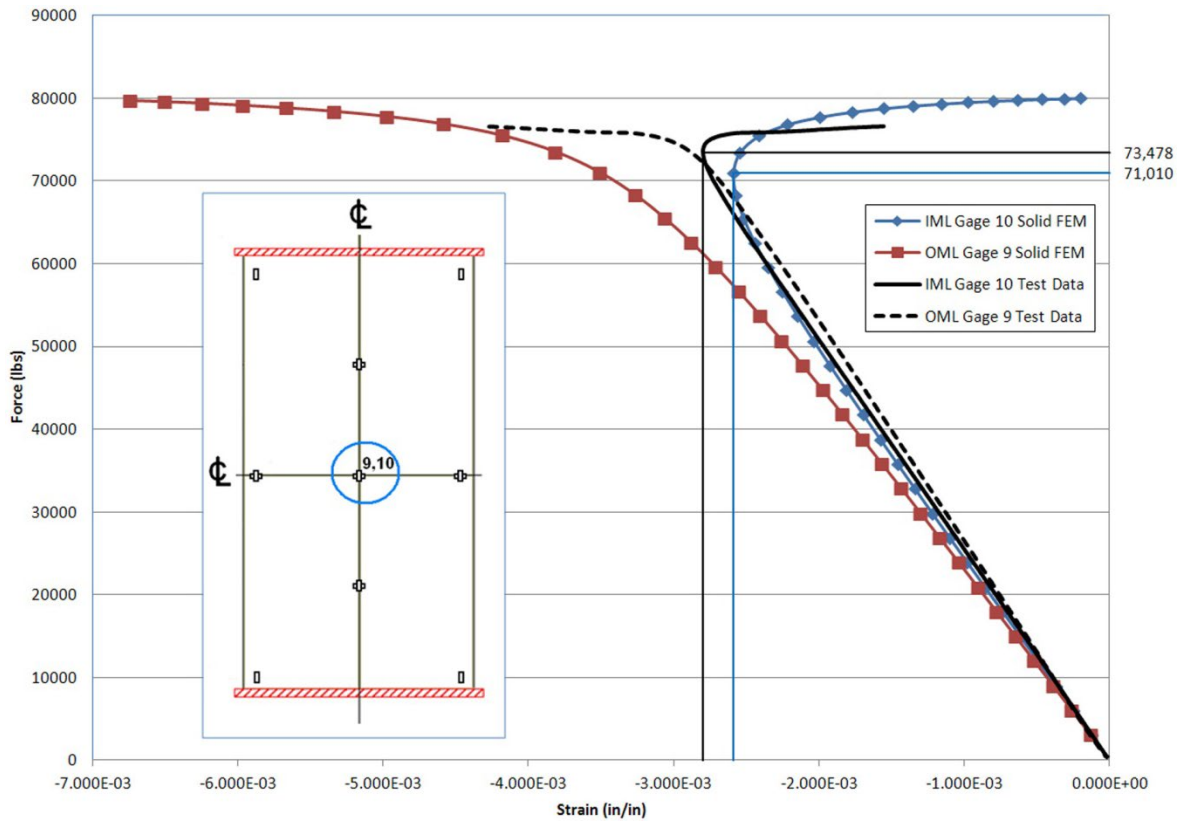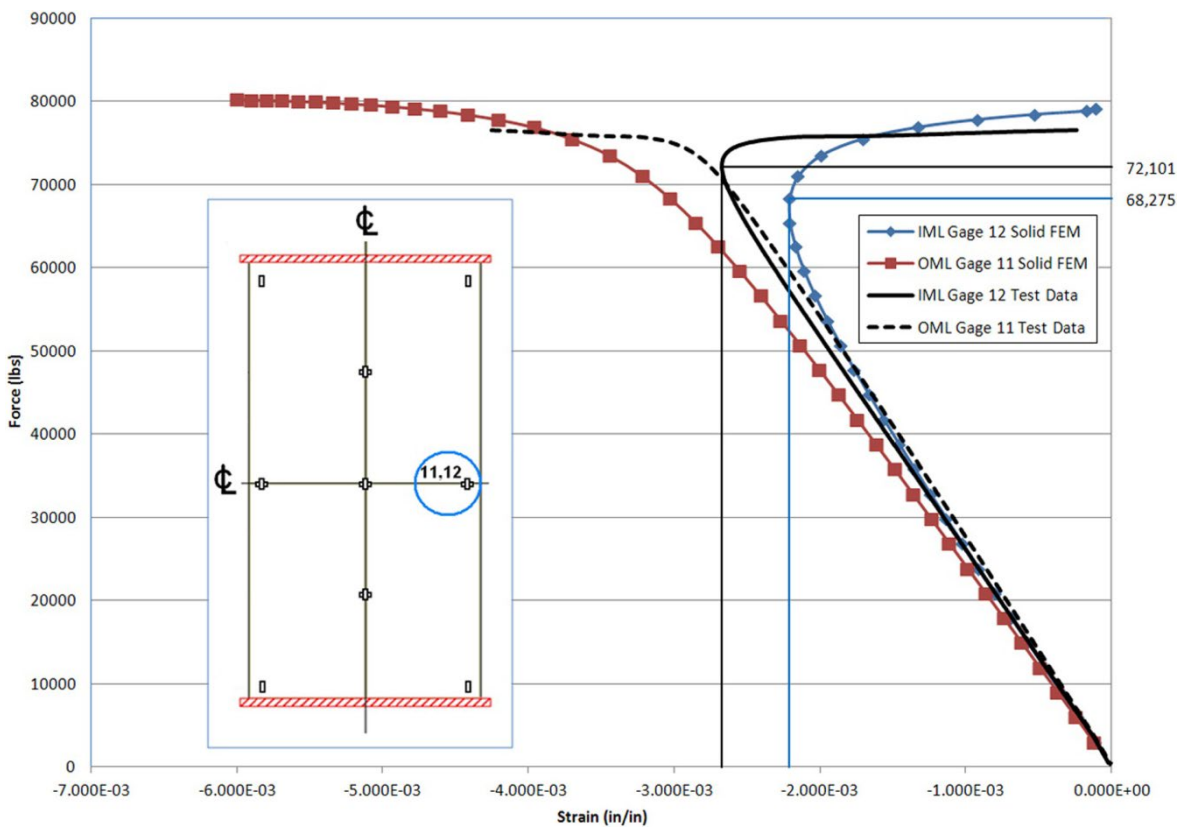ing success was evaluated using specifically defined criteria. Additionally, various parametric studies were performed to determine the impact of manufacturing defects, and modeling techniques.

In Section 1.2, the experimental success criteria were described, all of which were met. Namely, all critical instrumentation was fully operational during the test, loads were applied as described in this document, and the maximum attained load and all associated data were recorded and saved. Additionally, the modeling success criteria, described in Section 1.4 were also achieved: the buckling load was predicted within 20 percent, the buckling mode/direction was predicted correctly, and the local strain fields correlated well with visual imaging data measured during the experiment.

Both linear eigenvalue and geometrically nonlinear analyses were performed using a variety of commercially available FEM software tools to predict the buckling load of the honeycomb sandwich panel. The linear eigenvalue prediction fell within ~ 12 percent above the experimental buckling load. Surface imperfection measurements were introduced into the FEM model through a swept bow, and geometrically nonlinear analyses were utilized to predict the buckling load via progressive collapse simulations. The simulations yielded a buckling load prediction within ~5 percent higher than the experimental load. Furthermore, the direction of buckling (towards the I.D.) was predicted correctly, which was a direct consequence of including the measured geometric imperfections in the model. Full field displacement and strain measurements predicted with the nonlinear analysis also corresponded well qualitatively with experimental VIC data. Finally, linear strength analyses were completed at the buckling load, and they ensured that the predicted panel failure was driven by stiffness (i.e., buckling), not strength, as was observed in test.

A sensitivity study was enacted to determine the influence of geometric imperfections on the overall buckling behavior of the panel. Generic, arc-shaped bows were introduced into the models and used to represent the geometric imperfections. The magnitude of the largest deflection point was varied from 0.01500, 0.01600, 0.01700, 0.02000, to 0.03000 in. towards the I.D. It was discovered that the magnitude of the bow did not alter the stiffness of the panel but moderately influenced the buckling load and buckling direction. Applying a bow with a magnitude less than 0.01700 in. resulted in buckling towards the O.D., or the direction of major curvature, whereas, including a bow with a magnitude 0.01700 in. and higher led to buckling towards the I.D. (as observed in the experiment). The maximum buckling load was achieved at the transition point when the magnitude of the bow was 0.01700 in. The buckling load would increase as the magnitude of the bow was increased up to this point; however, increasing in the bow beyond 0.01700 in. yielded a decreasing buckling load.

An additional sensitivity study was carried out to investigate the effects of fiber misalignment on the panel response. Both panel stiffness and buckling load were found to be sensitive to small changes in the orientation of the 45° plies. It was concluded that using an angle of 46.5°, in lieu of all the 45° plies, led to the best agreement with the experiment. Moreover, if manufacturing tolerances are defined, a fiber misalignment study can be used to bound the numerical predictions.

It can be concluded that, a good buckling load prediction was achieved utilizing shell-based linear eigenvalue analysis in conjunction with nominal (perfect) panel geometry. This prediction was improved by utilizing a more sophisticated, geometrically nonlinear, progressive collapse analysis that incorporated measured geometric imperfections from the panel. Furthermore, sensitivity studies were used to quantify the effects of possible manufacturing defects on the performance of the panel. Although the results of these studies cannot be directly applied to obtain better estimates of the buckling loads (beyond eigenvalue analysis) of full cylinders or larger cylinder segments (as the buckling modes and imperfection sensitivities are different for these different geometries), the practices presented here can be used to determine the same sensitivities of these other structures to similar imperfections. In the future, such

studies may lead to more comprehensive linear bucking knockdown factors for cylindrical shells that consider the impact and degree of different imperfections or defects separately (Haynie et al., 2012; Hilburger, 2012; Kriegesmann et al., 2012). Furthermore, these sensitivity studies can be utilized to arrive at critical manufacturing tolerances.

References

ANSYS Mechanical Application User's Guide, Release 14.0, 2011 SAS IP, Inc.

Hause, T., Johnson, T. E., Librescu, L., Effect of face-sheet anisotropy on buckling and postbuckling of sandwich plates, Journal of Spacecraft and Rockets, 37(3), pp. 331-341, 2000.

Hause, T., Librescu, L., Johnson, T. F., Non-linear response of geometrically imperfect sandwich curved panels under thermomechanical loading, International Journal of Non-Linear Mechanics, 33(6), pp. 1039-1059, 1998.

Haynie, W. T., Hilburger, M. W., Bogge, M., Maspoli, M. Benedikt, K., Validation of lower-bound estimates for compression-loaded cylindrical shells, 53rd AIAA/ASME/ASCE/AHS/ASC Structures, Structural Dynamics, and Materials Conference, 23-26 Apr., Honolulu, HI, 2012.

Hilburger, M. W., Developing the next generation shell buckling design factors and technologies, 53rd AIAA/ASME/ASCE/AHS/ASC Structures, Structural Dynamics, and Materials Conference, 23-26 Apr., Honolulu, HI, 2012.

Hilburger, M. W., Nemeth, M. P., Starnes, J. H., Jr., Nonlinear and buckling behavior of curved panels subjected to combined loads, 42nd AIAA/ASME/ASCE/AHS Structures, Structural Dynamics and Materials Conference and Exhibit, 16-19 Apr., Seattle, WA, 2001.

Hilburger, M. W., Starnes, J. H., Jr., Effects of imperfections on the buckling response of compression-loaded composite shells, International Journal of Non-Linear Mechanics, 37, pp. 623-643, 2002.

Hong, C. S., Jun S. M., Buckling behavior of laminated composite cylindrical panel with initial imperfections, Winter Annual Meeting of the American Society of Mechanical Engineers, cosponsored by Pressure Vessels and Piping Division & Aerospace Division, ASME, San Francisco, CA, Dec. 10-15, 1989, PVP-Vol. 183, AD-Vol. 18.

HyperSizer Structural Sizing Software, Collier Research Corp., Newport News, VA, www.HyperSizer.com, 2012.

Jones, R. M., Mechanics of Composite Materials, 2nd Edition, Taylor & Francis, Inc., Philadelphia, PA, 1999.

Kellas, S., Lerch, B., Wilmoth, N., Mechanical characterization of in- and out-of-autoclave cured composite panels for large launch vehicles, SAMPE 2012, Baltimore, Maryland, May 21-24, 2012.

Kriegesmann, B., Hilburger, M. W., Rolfes, R., The effects of geometric and loading imperfections on the response and lower-bound buckling load of a compression-loaded cylindrical shell, 53rd AIAA/ASME/ASCE/AHS/ASC Structures, Structural Dynamics, and Materials Conference, 23-26 Apr., Honolulu, HI, 2012.

Ley, R. P., Lin, W., Mbanefo, U., Facesheet wrinkling in sandwich structures, NASA/CR—1999-208994, 1999.

Lockheed Martin, Orion Materials and Design Allowables, Rev. D, 22 Sept, 2010.

Lynch, C., Murphy, A., Price, M., Gibson, A., The computational post buckling analysis of fuselage stiffened panels loaded in compression, Thin-Walled Structures, 42, pp. 1445-1464, 2004.

Schultz, M. R., Nemeth, M. P., Buckling imperfection sensitivity of axially compressed orthotropic cylinders, 51st AIAA/ASME/ASCE/AHS/ASC Structures, Structural Dynamics, and Materials Conference, 12-15 Apr., Orlando, FL, 2010.

Singer, J., Arboz, J., T. Weller, Buckling Experimental Methods in Buckling Thin Walled Structures, Basic Concepts, Columns, Beams and Plates—Volume 1, John Wiley & Sons, Inc., New York, 1998.

Vinson, J. R., The Behavior of Sandwich Structures of Isotropic and Composite Materials, Technomic Publishing Co., Lancaster, PA, 1999.

Zalewski, B. F., Dial, W. B., Bednarcyk, B. A., Methods for assessing honeycomb sandwich panel wrinkling failures. NASA/TM—2012-217697, 2012.

REPORT DOCUMENTATION PAGE				*Form Approved* *OMB No. 0704-0188*
The public reporting burden for this collection of information is estimated to average 1 hour per response, including the time for reviewing instructions, searching existing data sources, gathering and maintaining the data needed, and completing and reviewing the collection of information. Send comments regarding this burden estimate or any other aspect of this collection of information, including suggestions for reducing this burden, to Department of Defense, Washington Headquarters Services, Directorate for Information Operations and Reports (0704-0188), 1215 Jefferson Davis Highway, Suite 1204, Arlington, VA 22202-4302. Respondents should be aware that notwithstanding any other provision of law, no person shall be subject to any penalty for failing to comply with a collection of information if it does not display a currently valid OMB control number. PLEASE DO NOT RETURN YOUR FORM TO THE ABOVE ADDRESS.				

1. REPORT DATE *(DD-MM-YYYY)*
01-04-2013

2. REPORT TYPE
Technical Memorandum

3. DATES COVERED *(From - To)*

4. TITLE AND SUBTITLE
Buckling Testing and Analysis of Honeycomb Sandwich Panel Arc Segments of a Full-Scale Fairing Barrel
Part 1: 8-Ply In-Autoclave Facesheets

5a. CONTRACT NUMBER

5b. GRANT NUMBER

5c. PROGRAM ELEMENT NUMBER

6. AUTHOR(S)
Myers, David, E.; Pineda, Evan, J.; Zalewski, Bart, F.; Kosareo, Daniel, N.; Kellas, Sotiris

5d. PROJECT NUMBER

5e. TASK NUMBER

5f. WORK UNIT NUMBER
WBS 432938.11.01.03.02.01.06

7. PERFORMING ORGANIZATION NAME(S) AND ADDRESS(ES)
National Aeronautics and Space Administration
John H. Glenn Research Center at Lewis Field
Cleveland, Ohio 44135-3191

8. PERFORMING ORGANIZATION REPORT NUMBER
E-18570

9. SPONSORING/MONITORING AGENCY NAME(S) AND ADDRESS(ES)
National Aeronautics and Space Administration
Washington, DC 20546-0001

10. SPONSORING/MONITOR'S ACRONYM(S)
NASA

11. SPONSORING/MONITORING REPORT NUMBER
NASA/TM-2013-217822-PART1

12. DISTRIBUTION/AVAILABILITY STATEMENT
Unclassified-Unlimited
Subject Categories: 15, 18, 24, 26, 37 and 39
Available electronically at http://www.sti.nasa.gov
This publication is available from the NASA Center for AeroSpace Information, 443-757-5802

13. SUPPLEMENTARY NOTES

14. ABSTRACT

Four honeycomb sandwich panels, representing 1/16th arc segments of a 10-m diameter barrel section of the heavy lift launch vehicle, were manufactured under the NASA Composites for Exploration program and the NASA Space Launch Systems program. Two configurations were chosen for the panels: 6-ply facesheets with 1.125 in. honeycomb core and 8-ply facesheets with 1.000 in. honeycomb core. Additionally, two separate carbon fiber/epoxy material systems were chosen for the facesheets: in-autoclave IM7/977-3 and out-of-autoclave T40-800b/5320-1. Smaller 3.00- by 5.00-ft panels were cut from the 1/16th barrel sections. These panels were tested under compressive loading at the NASA Langley Research Center. Furthermore, linear eigenvalue and geometrically nonlinear finite element analysis was performed to predict the compressive response of the 3.00- by 5.00-ft panels. This manuscript summarizes the experimental and analytical modeling efforts pertaining to the panel composed of 8-ply, IM7/977-3 facesheets (referred to Panel A). To improve the robustness of the geometrically nonlinear finite element model, measured surface imperfections were included in the geometry of the model. Both the linear and nonlinear models yield good qualitative and quantitative predictions. Additionally, it was predicted correctly that the panel would fail in buckling prior to failing in strength. Furthermore, several imperfection studies were performed to investigate the influence of geometric imperfections, fiber misalignments, and three-dimensional (3-D) effects on the compressive response of the panel.

15. SUBJECT TERMS
Fiber composites; Polymer matrix composites; Carbon fiber reinforced plastics; Computational mechanics; Sandwich structures; Buckling; Nonlinearity; Collapse; Launch vehicles; Spacecraft structures

16. SECURITY CLASSIFICATION OF:

a. REPORT	b. ABSTRACT	c. THIS PAGE
U	U	U

17. LIMITATION OF ABSTRACT
UU

18. NUMBER OF PAGES
46

19a. NAME OF RESPONSIBLE PERSON
STI Help Desk (email:help@sti.nasa.gov)

19b. TELEPHONE NUMBER *(include area code)*
443-757-5802